X-ray microtomography of materials

S. R. Stock

X-ray microtomography allows imaging of the interior microstructure of materials non-destructively and with spatial resolution which can approach that of optical microscopy (typically, no better than 1 μm in samples whose cross-sectional diameter is on the order of 1 mm, and 10 μm for 10 mm specimens). First, X-ray microtomography's origin in medical imaging and the physics behind computed tomography are reviewed. Summaries of apparatus, radiation sources, data collection schemes, and of materials applications follow. To date, most materials applications fall into one of four areas: inorganic matrix composites, transport in porous media, calcified tissue, and fatigue crack closure. Details of studies in each area highlight the advantages X-ray microtomography brings, and the final section focuses on future directions suggested by recent work using imaging modalities other than X-ray attenuation. IMR/343

Introduction

The present review is 'more and more about less and less'.[1] While this approach is undesirable in rhetoric or prose, many materials science/engineering advances resulted from following this precept: delving into ever finer microstructural scales in order to explain macroscopic behaviour of materials. One of the ways of learning more and more about less and less, X-ray computed tomography, offers the additional advantage of being non-invasive and non-destructive. That is, the same object can be reinstalled after inspection or the same sample can be interrogated multiple times during the course of mechanical or other testing.

X-ray computed tomography is quite familiar in its medical manifestations (CT, CAT scans, etc.), but it is less known as an imaging modality for components or materials. Computed tomography provides an accurate map of the variation of X-ray absorption within an object, regardless of whether there is a well defined substructure of different phases or slowly varying density gradients. High resolution X-ray computed tomography is also termed microtomography and reconstructs samples' interiors with the spatial and contrast resolution required for many problems of interest, and the application of microtomography to materials science/engineering problems is the subject at hand. The division between conventional computed tomography and microtomography is, of course, an artificial distinction, but here microtomography is taken to include results obtained with at least 50–100 μm spatial resolution. The actual resolution needed for a particular application depends on the microstructural features of interest and their shapes.

After presenting the author's perspective of the development of microtomography, imaging, X-ray attenuation, and the physical concepts underlying computed tomography are reviewed. Data collection strategies, radiation sources, and detectors are summarised in the third section. The fourth section describes how microtomography has been applied to several classes of materials problems. Speculation concerning future directions concludes the review.

Background

It is hard to know whether the theft of ideas, themes, concepts, etc. is more important in popular culture (or in the fine arts for that matter) or in science and engineering. Because the subject here is how high resolution X-ray computed tomography has been and can be applied in the field of materials, 'theft' is not used in its ethical sense, but rather in the loose sense of appropriations of an approach from a very different field. The applications of X-radiation exemplify the process.

No sooner had Röntgen discovered X-radiation than he applied the new found penetrating radiation to radiological imaging – the first widespread publication of the discovery of X-rays featured a radiological image.[2] Within 20 years this new medical tool was in use across the battlefields of the First World War.[3] Locating projectiles and shrapnel and checking the reduction of fractures non-invasively was a true breakthrough. One of the advantages of radiological images or radiographs, simplicity, can also be a severe limitation: these images are nothing more than two-dimensional projections of the variation of X-ray absorptivity within the object under study. While recording stereo pairs allows precise three-dimensional location of high contrast objects, this approach is impractical when a large number of similar objects produce a confusing array of overlapping images or when there are no sharp charges of contrast on which one can orient.

A strategy for recovering three-dimensional internal structure evolved prior to digital computers.[4] It involves translating the patient (or object to be imaged) together with the detection medium (film or other two-dimensional detector) in such a way that only one narrow slice parallel to the translation plane remains in focus and is termed laminography or focal plane tomography.[*,5,6] The contrast from features outside of this slice is blurred to the point that it disappears from the image. Sharp images are

---

*The word tomography arises from the Greek *tomos* for slice, section, or cut, as in common medical usage such as appendectomy, plus 'graphy'[5] and appears in print as early as 1935.[6]

difficult to obtain, in part, because of the thickness of each slice; and the smearing of images outside the imaging 'plane' across the image of the plane of interest seriously degrades contrast within the slice. Laminography continues to be used as an inspection tool for objects whose geometry is impractical for computed tomography, e.g. relatively planar objects such as printed wiring boards.

Computed tomography, an approach superior to laminography for most applications, became possible with the development of digital computers. Radon[7] established the mathematics underlying computed tomography in 1917, and in 1968 Cormack[8] demonstrated the feasibility of using X-rays and a finite number of radiographic viewing directions to reconstruct the distribution of X-ray absorptivity within a cross-section of an object. Early in the 1970s Hounsfield[9] developed a commercial computed tomography system for medical imaging, and the number of medical systems is now virtually uncountable.

In computed tomography of patients there are several constraints which affected the way in which apparatus were developed. First, the dose of X-rays received by the patient must be kept to a minimum. Second, the duration of data collection must be limited to several seconds to prevent involuntary patient movement from blurring the image. These considerations do not apply in general to imaging of inanimate objects, and longer data collection times can be used to improve the signal/noise ratio in the data. Early on, engineering components and assemblies were characterised by medical computed tomography scanners but, because the medical systems were optimised for the range of contrast encountered in the body and not for objects of technological interest, systems for non-destructive evaluation and materials characterisation were soon marketed. In terms of the metaphor with which this section began, the circle of thefts from physical science to medicine to physical science/engineering was complete.

Industrial X-ray computed tomography has gained a measure of acceptance,[10,11] but the high cost of the instrumentation means that it will not replace X-radiography in many non-destructive evaluation applications. Applications where X-ray computed tomography offers significant economic advantages include five areas:[11] new product development, process control, non-invasive metrology, materials performance prediction, and failure analysis. The information computed tomography provides can drastically shorten the iterative cycles of prototype manufacture and testing required to bring new manufacturing processes under control. Evaluation of castings by radiography is very time consuming because of widely varying thicknesses of these components while computed tomography allows relatively inexpensive inspection; with accurate three-dimensional tomographic measurements, castings with critical flaws can be eliminated before subsequent costly manufacturing steps and those with anomalies such as voids that can be demonstrated to be non-critical can be retained and not scrapped. Integrating computed tomography data of as manufactured components into structural analysis programs seems very promising, particularly for anisotropic materials such

as metal matrix composites.[12] Final assembly verification, for example in small jet engines, is a third area where computed tomography appears to be cost effective.

The extreme sensitivity of X-ray computed tomography to density charges can be exploited to follow damage propagation in polymeric matrix composites,[13] even when the microcracks produced cannot be resolved by the most sensitive X-ray imaging techniques. X-ray computed tomography can be performed with a portable unit and offers considerable promise for studying the processes active in growing trees and for milling lumber: the environmental effects on a forest of a nearby chemical or power plant can be assessed over a number of years on the same set of trees, daily and seasonal changes in the cross-sectional distribution of water can be obtained and luck can be removed from the process of obtaining large wooden panels with beautiful ring patterns and without knots or decay.[14,15] Pyrometric cones used for furnace temperature calibration are produced in the millions annually and in at least 100 compositions, and X-ray computed tomography has been applied to understand why certain powder compositions for these dry pressed, self-supporting cones produce large density gradients in dies and rejections rates (due to fracture) several times higher than most other compositions.[16] Of interest also is comparative work using magnetic resonance imaging and X-ray computed tomography to study ceramics.[17]

As with any other imaging modality, new applications required resolution of even smaller features, and this became the goal of one branch of workers in computed tomography. If instead of resolving features with dimensions barely smaller than millimetres, as is typical of industrial computed tomography equipment, one were able to image features on the scale of 10 µm, then many microstructural features in engineering materials could be studied non-destructively. This size scale is also important in biological structural materials such as calcified tissue. Areas in which microtomography has been employed profitably include damage accumulation in composites, fatigue crack closure in metals, and densification of ceramics.

One can view the advances in microtomographic imaging since the 1980s as a by-product of the demand for improved area detectors for consumer electronics. Before considering the mathematics and physics of computed tomography and the hardware requirements for microtomography, it is constructive to review the early chronology of microtomography (or at least the author's perspective of how this developed). The first realisation of microtomography seems to have been in 1982;[18] and, until recently, this group has used a microfocus X-ray source and a pinhole collimator to collect high resolution data.*,[19] In work published in 1983, Grodzins[20,21] suggested how using the *tunability* of synchrotron X-radiation would allow one to obtain enhanced contrast from a particular

---

* Sato *et al.*[19] presented reconstructions of an optical fibre, claiming 20 µm spatial resolution but, due to the noise in the image and the unfortunate sample geometry, it appears to the author that the reconstructions are dominated by reconstruction artefacts.

element within a sample imaged with computed tomography, namely by comparing a reconstruction from data collected at a wavelength below that of the absorption edge of the element in question with a reconstruction from a wavelength above the edge. In 1984, Thompson *et al.*[22] published low resolution computed tomography results using synchrotron radiation and the approach advocated by Grodzins. Within a few years multiple groups had demonstrated microtomography using synchrotron radiation[23–33] while others applied X-ray tube based microtomography.[34–38] It is important to emphasise the shift from collecting single slices to collecting volumetric (i.e. simultaneously collected multiple adjoining slices) data.

Physics and mathematics of computed tomography

The fundamentals of computed tomography have been summarised numerous times,[10,12,39–47] and, keeping with the task at hand, only those details are presented which are required to appreciate the published applications of X-ray microtomography. The nomenclature used below follows that of ASTM E1441-95.[40] First, the interaction of X-rays with matter will be covered. Next the physical concepts involved in reconstructing objects will be reviewed followed by a brief foray into the mathematics of the process. Finally, practical details including sampling considerations, various data collection strategies, and available detectors close the discussion.

The visibility of the various features of an object depend on the spatial resolution with which they may be imaged and on the contrast the features have relative to their surroundings. Understanding the interplay of contrast sensitivity and spatial resolution is important to appreciating what can be achieved with computed tomography.

Contrast is a measure of how well a feature can be distinguished from the neighbouring background. Frosty the Snowman's eyes of coal show high contrast while writing with a yellow highlighter marker on a white sheet of paper provides little contrast. It is important to be able to quantify the amount of contrast present in an objects' image because the smallest change in contrast which can be reliably discerned by the imaging system dictates quantities like detection limits. Contrast is often defined in terms of the ratio of the difference in signal between feature and background to the signal from the background. Thus the fractional contrast is given by

$$\text{contrast} = \frac{|\text{sig}_f - \text{sig}_b|}{\text{sig}_b} \qquad \ldots \ldots \ldots (1)$$

where sig is the signal observed from the object and whose point by point variation makes up the image and the subscripts f and b denote feature and background respectively.

Spatial resolution describes how well small details can be imaged or small features can be located with respect to some reference point. One generally quantifies spatial resolution in terms of the smallest separation at which two points can be perceived as discrete entities. Regardless of the criteria adopted for spatial resolution, instrumental factors such as penumbral blurring (Fig. 1) from a finite light or X-ray source size act to limit the resolution which can be obtained. The amount of background and of noise influence the spatial resolution with which identical point-like features can be reliably imaged. For example, a pair of high contrast features can be differentiated at a smaller separation than the same sized low contrast features.

The presence of noise and inherent imaging imperfection means that quantities such as apparatus performance and image fidelity must be measured in probabilistic terms for a given set of imaging conditions. The point spread function (PSF), for example, describes how the system responds to a point input (i.e. how it images a point), and the modulation transfer function (MTF) represents the interaction of the system (PSF) with multiple features of the object being imaged (i.e. the convolution of all these factors). The number of line pairs mm^{-1} which can be resolved is an often used simplification. A more accurate approach, reflecting the fact that features must be both detected and resolved, is plotting the contrast required for 50% discrimination of pairs of features as a function of their diameters in pixels; this is termed the contrast–detail–dose curve.[40]

As discovered by Röntgen,[2] the attenuation of X-rays of wavelength λ is given for a homogeneous object by the familiar equation[48]

$$I/I_0 = \exp(-\mu x) \qquad \ldots \ldots \ldots \ldots \ldots (2)$$

where I_0 is the intensity of the unattenuated X-ray beam, and I is the beam's intensity after it traverses a thickness of material x characterised by a linear attenuation coefficient μ. Typically one finds μ given in cm^{-1}. Rewriting equation (1) in terms of the mass attenuation coefficient μ/ρ (units cm^{-2} g^{-1}) explicitly recognises that the fundamental basis of the amount of attenuation is the number of atoms encountered by the X-ray beam

$$I/I_0 = \exp[(-\mu/\rho)\rho x] \qquad \ldots \ldots \ldots (3)$$

Equations (2) and (3) reveal what is observed after attenuation is complete, and writing the differential form focuses attention on what occurs within each small thickness element dx

$$\frac{\mathrm{d}I}{I} = -\frac{\mu}{\rho}\rho \, \mathrm{d}x \qquad \ldots \ldots \ldots \ldots (4)$$

The size of dx into which the path can be segmented varies from instrument to instrument and sample to sample but, on the scale of the minimum realistic thickness element dx, $(\mu/\rho)\rho$ is regarded as a constant and is written simply as μ. Adding the increments of the attenuation along the direction of X-ray propagation yields the more general form

$$I = I_0 \exp\left[-\int \mu(s) \, \mathrm{d}\mathbf{s}\right] \qquad \ldots \ldots \ldots (5)$$

where $\mu(s)$ is the linear absorption coefficient at position s along ray $\mathbf{s}$. Assigning the correct value of μ to each position along this ray (and along all the other rays traversing the sample) knowing only the values of the line integral for the various orientations

(a)   (b)
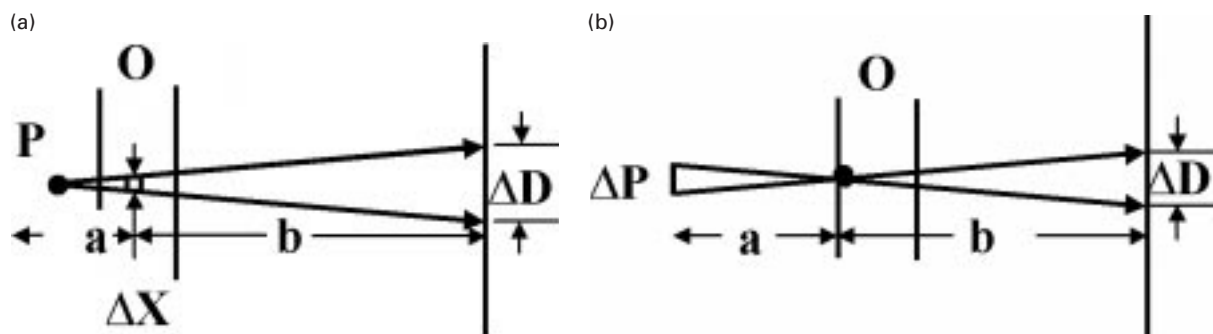
1   Illustration of *a* geometrical magnification and *b* penumbral blurring. In geometrical magnification, divergent beam from point source P spreads sample feature at O with width Δ*x* to width Δ*D* on detector or film plane. Amount of magnification depends on ratio of object to detector separation *b* source to object separation *a*. Penumbral blurring occurs when there is finite source size Δ*P* at distance *a* from point-like feature O in sample. Crossfire from source spreads contrast from O and Δ*D* on detector or film *b* from object. In both cases trigonometry is all that is required to calculate amount of magnification or level of blurring.

of **s**, i.e.

$$\int \mu(s)\,\mathrm{d}\mathbf{s} = \ln(I_0/I) \quad \ldots \ldots \ldots \ldots \quad (6)$$

is the central problem of computed tomography.

Locating and defining the different contributions to attenuation requires measuring I/I_0 for many different ray directions **s**. Measuring I/I_0 for many different positions for a given **s** is also required: a radiograph measures exactly this quantity, the variation of I/I_0 as a function of position for a given projection or ray direction. Thus, a set of high resolution radiographs collected at enough well chosen directions **s** can be used to reconstruct the volume through which the X-rays traverse.

The reality of being able to reconstruct volumes can be illustrated simply by considering how the profile or projection of X-ray attenuation $P(\mathbf{s})$ from a simple object changes with viewing direction. The low absorption rectangle within the slice pictured in Fig. 2 casts a spatially narrow but deep 'shadow' in the attenuation profile seen along one viewing direction and a spatially wide and shallow 'shadow' along the second viewing direction. For the views parallel to the sides of the rectangle, the corresponding changes in the profile are quite sharp but, for views oriented midway between the two pictured in Fig. 2, the changes in the profile would be more complex. For this simple case the two correctly chosen views suffice to define the location of the rectangle and the change of μ between the cylinder and rectangle. Recording radiographic stereo pairs is often used to precisely triangulate sharply defined features, i.e. views of the same sample are recorded along two view directions separated by a precisely known angle between 5 and 10°. This very rapid approach to three-dimensional inspection is of little use and gives way to computed tomography when there are so many similar overlapping objects that individuals cannot be distinguished, when contrast does not vary sharply within the sample, or when the features to be imaged are so *anisotropic* that they produce significant contrast only along certain viewing directions which cannot be determined *a priori* (e.g. a crack).

In understanding the various experimental approaches to microtomography, it helps first to consider the requirements for reconstructing an $M \times M$ object (i.e. a planar slice through an object consisting of $M \times M$ volume elements or voxels). A set of systematically sampled line integrals $\ln(I_0/I)$ must be measured over the entire cross-section of interest such that the geometrical relationship between these measurements is precisely defined. The quality of reconstruction depends on how finely the object is sampled (i.e. the spatial frequencies resolved in the profiles $P(\mathbf{s})$ and the number of viewing directions), on how accurately individual measurements of $\ln(I_0/I)$ are made (i.e. the levels of random and
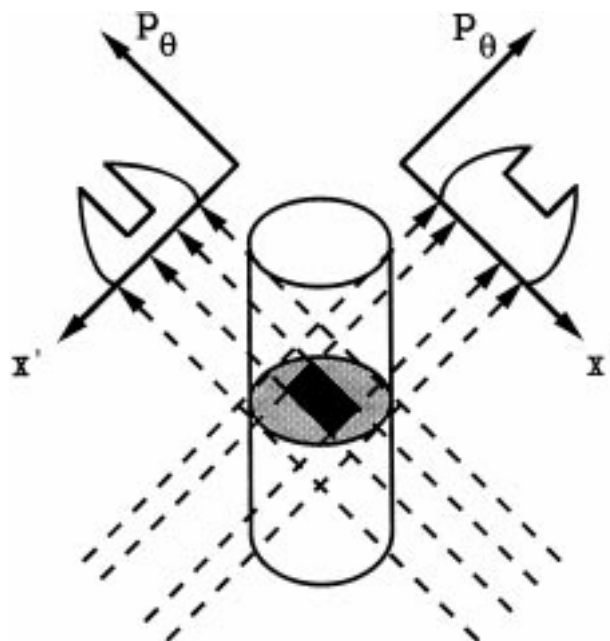
2   Illustration of how internal structure of objects can be determined from projections. For simplicity only single plane and parallel X-radiation are pictured, and rotation axis for collecting views (i.e. absorption profiles P_θ) along different directions θ is vertical and in centre of cylindrical sample.[43] © ASME
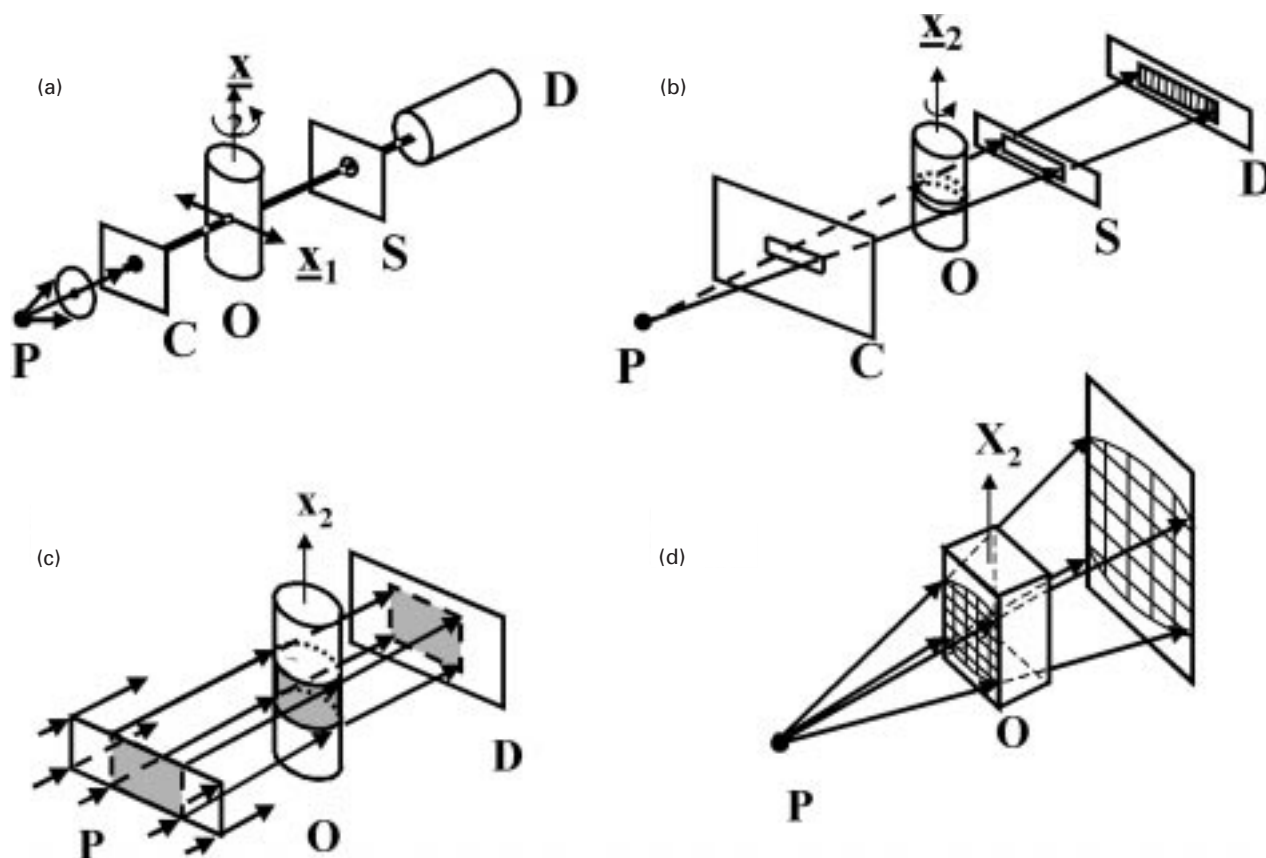
3 Illustration of four experimental approaches to X-ray microtomography data collection: *a* pencil, *b* fan, *c* parallel, and *d* cone beam methods. P is X-ray source, C is collimator, O is object being imaged, x_2 is axis about which sample is rotated to produce different views required for reconstruction, S is slit, and D is detector

systematic errors), and on how precisely each measurement can be related to a common frame of reference.

The number of samples per projection and the number of views needed depends on the reconstruction method and on the size of features one wishes to resolve in the reconstruction. For an $M \times M$ slice, a minimum of $(\pi/4)M^2$ independent measurements are required for noise-free data, but faithful reconstruction can still be obtained with sampling approaching this minimum, even in the presence of noise.[40] Features down to one-tenth of the reconstructed voxels can be seen if contrast is high enough,[41,49] and metrology algorithms can measure dimensions to about one-tenth of a pixel with a three sigma confidence level. The number of samples per view is generally more important than the number of views, errors in I/I_0 of 10^{-3} have been found to be significant,[50] and both place important constraints on detectors for computed tomography. Summarising the variety of reconstruction algorithms falls outside the scope of the present review (*see* for example Refs. 39 and 40), and public domain libraries of reconstruction software are available.[51]

All of the 'exact' reconstruction algorithms require a full 180° set of views although approximate reconstructions can be obtained where views are missing, for example where opacity and sample size limits the directions along which useful views may be obtained;[52,53] the cost is a degraded quality recon-

struction. Another approximate data collection approach is spiral tomography,[54,55] and it has received considerable attention because it affords increased speed and lower patient X-ray dosage. Only those details important in a particular data collection strategy and those reconstruction artefacts important in the examples will be discussed.

Apparatus, radiation sources, and data collection

Most microtomography systems employ one of four geometries. While two arrangements are the same as two of the four generations of scanners into which the computed tomography literature classifies apparatus, the other two are different.

In first generation or pencil beam systems (Fig. 3*a*), a pinhole collimator C from point-like source P produces a narrow, pencil-like beam which is scanned across the object O along x_1 to produce each view; successive views are obtained by rotation about x_2. Only a simple zero-dimensional X-ray detector D is required, perhaps with some scatter shielding S, and energy sensitive detectors are readily available and, if used instead of gas proportional or scintillation detectors, allow reconstructions to obtain very accurate values of the linear attenuation coefficients. Successive views are obtained by rotating the sample and repeating the translation. Obtaining volumetric data (i.e. a set of adjacent slices) borders on infeasible because of

the long scan times required, but this is balanced by the inherent simplicity and flexibility of such apparatus and by a relatively greater immunity to degradation of contrast due to scatter. Pencil beam microtomography continues to be used with laboratory X-ray sources,[18,56–69] and very high spatial resolution has been achieved in small samples using synchrotron radiation.[27,70,71]

Fan beam systems (Fig. 3*b*, that is, third generation apparatus) use a rotate-only geometry. A flat fan of X-rays defined by C and spanning the sample originates at the point-like source P, passes through the sample and scatter shield S and is collected by the one-dimensional X-ray detector. These systems are often used with laboratory microfocus generated X-radiation. This detector consists of an array of discrete elements which allows the entire view to be collected simultaneously. One to two thousand detectors are typically in the array, making fan beam systems much more rapid than pencil beam systems, but data for only one slice are recorded at a time. The necessity of normalising detector response is introduced and ring artefacts can result from various non-uniformities. For example, incorporating a linear or area detector makes the system become much more susceptible to scatter (than pencil beam systems), that is, the redirection of photons from the detector element on a line of sight from the X-ray source into another detector element. In severe cases, this can greatly affect the fidelity of a reconstruction. Further, it is necessary to normalise the response of the different detector elements; even with careful correction, ring artefacts from various non-uniformities can still appear in reconstructions. When examining slices from fan beam systems it is not only important to note the dimensions of the pixels in the plane of reconstruction, it is also important to ascertain the thickness of the slice. Systems collecting data for one slice at a time often are used with a detector width (perpendicular to the reconstruction plane) and slice thickness substantially larger than the voxels' dimensions in the reconstruction plane. This certainly improves signal/noise ratio in the reconstruction and is very effective when samples with slowly varying structure along one axis are imaged with this axis perpendicular to the reconstruction plane.[72] This approach sacrifices sensitivity to defects much smaller than the slice thickness.

In situations where a spatially-wide, parallel beam of X-rays is available, the parallel beam geometry (Fig. 3*c*) allows straightforward and very rapid data collection for multiple slices (i.e. a volume) simultaneously. A parallel beam from a source P (with a certain cross-sectional area) shines through the sample and is collected by a two-dimensional detector array. Since the X-ray beam is parallel, the projection of each slice of O on D (i.e. each row of the array) is independent of all other slices. In practice, this must be done at storage rings optimised for the production of the hard synchrotron X-radiation.[24,26] High performance area detectors are required, but there is an enormous increase in data collection rates over the geometries described above. Because most area detectors consist of a square array of detector elements, slices are generally, but not always, reconstructed

with isotropic voxels (i.e. the voxel dimensions within the reconstruction plane equal the slice thickness).

The cone beam geometry (Fig. 3*d*), the three-dimensional analogue of the two-dimensional fan beam arrangement, is a fourth option; it is especially well suited for volumetric computed tomography employing microfocus tube sources.[36–38] The X-rays diverge from the source, pass through the sample, and are recorded on the area detector. In this geometry each detector row, except the central row, receives contributions from more than one slice, and the effect becomes greater the farther one goes from the plane perpendicular to the rotation axis. The cone beam reconstruction algorithm is an approximation, however, and some blurring is to be expected in the axial direction for features which do not have significant extent along this direction. Nonetheless, reconstruction of the same 8 mm cube of trabecular bone from data collected with orthogonal rotation axes show only minor differences when the same slices are compared.[38] With an X-ray source size approaching 5–10 μm, system resolution is limited by that of the X-ray detector array and can be better than 50 μm. Note that only the portions of the sample which remain in the beam throughout the entire rotation can be reconstructed.

In synchrotron based microtomography, the cost of discarding most of the X-ray spectrum during monochromatisation is insignificant compared to the times required for sample movement, detector readout, etc. In most cases the resulting monochromatic beam is intense enough for a view to be collected in 1 s or less. As mentioned earlier, collecting microtomography data above and below the absorption edge of an element of interest and comparing the two reconstructions provides considerably improved sensitivity.[73,74] Most microtomography with tube sources of X-radiation has been performed using the entire spectrum, Bremsstrahlung and characteristic radiation, because the cost in data collection times is prohibitive in this photon starved environment. Exceptions include studies done with pencil beam systems. One group used an energy sensitive detector to correct for polychromaticity[65] and another used a channel cut monochromator.[69]

The use of polychromatic radiation produces an effect called beam hardening: the average photon energy of the beam penetrating the sample increases with increasing sample thickness because the lower energy photons are absorbed at a much higher rate than the higher energy photons. Thus equations (1)–(5) are no longer strictly valid as written. Beam hardening combined with scattering leads to cupping in reconstructed slices of a uniform object, that is, a radial gradient in μ with abnormally low values at the interior centre and high values at the periphery. Dual energy techniques, however, offer promise of correcting for the effect of collecting data using a range of wavelengths.[75]

The characteristics of the X-ray detector array used have important consequences for the performance of a given microtomography apparatus. Most one- or two-dimensional detector arrays are based on semiconductor devices (e.g. photodiode arrays, charge injection devices, and charge coupled devices (CCDs))

which work efficiently with optical photons and which are not suitable as direct X-ray detectors. These detectors are quite transparent at photon energies above 10 keV and quickly suffer radiation damage. Instead of detecting the X-ray photons directly, the array is coupled to an X-ray sensitive media chosen for optimum performance for the X-ray energies of interest. These media scintillate when X-ray photons are absorbed.

The size of the X-ray source affects the spatial resolution which can be obtained. This is normally not a consideration with synchrotron radiation, given the intrinsic low divergence and the typical source to sample distances employed (>10 m). With X-ray tubes, using a small (5–10 μm) dia. X-ray source limits the loading of the target (i.e. the amount of energy which may be deposited) and the resulting X-ray intensity. This must be balanced against use of a larger spot size where penumbral blurring would prevent small features from being seen. As will be discussed in the context of quantification of crack openings in the applications section, there are situations where much can be done even in the presence of significant penumbral blurring.

Most groups engaged in microtomography based their apparatus on linear or area detectors because volumetric work is largely impractical with pencil beam systems. Details typical of pencil beam systems appear elsewhere,[64] and the discussion here will, therefore, focus on one- and two-dimensional detectors. Besides the electronics necessary to read the linear or area detectors, these systems consist of an X-ray sensitive medium (phosphor) for converting the incident X-rays into a signal (generally light) which can be coupled (lens system or fibre optic channel plate) to the detector array.

One-dimensional photodiode arrays (Reticon devices, typically 1024 elements) have been successfully used in several single slice microtomography apparatus.[28,29,33–35,72,76] In these systems, optical fibres are typically used to couple the detector with the phosphor. Some systems have Gd_2O_2S/Tb based phosphors coated directly on the end of the fibres, while another couples to a 650 μm thick transparent layer in which 4 μm dia. particles are embedded.[29] As is noted elsewhere,[45] photodiode arrays are quite noisy and suffer from significant non-linearities which can lead to very serious ring artefacts in reconstruction.

Some two-dimensional detector systems have been based on vidicons,[36–38,77–79] but most are based on two-dimensional CCDs. Within each device (metal oxide silicon (MOS)) of the CCD array, an absorbed photon creates a charge pair. The electrons are accumulated in each detector well during exposure, and the individual detector elements are read digitally by transferring charge from pixel to pixel until all columns of pixels have reached the readout register and been stored in the computer system. The larger the detector element area, the greater the number of electrons which can be stored and the greater the dynamic range. Normally one thinks of increased detector element size entailing a sacrifice of spatial resolution, but this need not be so if the number of detector elements sampling the specimen cross-section

remains constant. Table 1 gives typical formats, pixel sizes, and dynamic ranges of some of the CCDs used in microtomography.[45,80–82] Efforts to develop large detector arrays composed of a mosaic of CCD chips are also of interest.[83]

The characteristics of the X-ray to light conversion media dictate, to a large extent, what coupling scheme is optimum for a given area detector.[84,85] Phosphor powders on a screen or embedded in transparent media,[23,24,28] monolithic or fibre optic scintillator glasses,[81] single crystal scintillators,[45] and lithographically fabricated cellular phosphor array consisting of 2·5 μm spaced close packed holes filled with plugs of phosphor[26] have been used. All of the phosphor 'screens' except the last can be obtained in a straightforward fashion, and the reason for going to such extremes in producing a discretised micrometre scale fluorescent screen was to prevent optical crosstalk between adjacent detector elements.[25] The noise from scatter, however, remains, and little seems to be gained comparatively by the discretisation.[45] Bonse et al.[80] compare the performance of two X-ray to light converters, a $CdWO_4$ single crystal plate 0·5 mm thick, and an Y_2O_2S/Eu screen about 40 μm thick and note that the screen was up to $\times 15$ greater in fluorescence while the single crystal provided considerably better spatial resolution (80 line pairs mm^{-1} at 20% contrast, corresponding to 6 μm resolution). Bueno et al.[81] compared several commercial inorganic polycrystalline phosphor screens to fibre optic glass scintillator arrays and report better performance with the glass (up to 20 line pairs mm^{-1}) than the powder scintillators. Corrections for various inhomogeneities are required.[86,87]

Microchannel plates have found use coupling powder scintillator screens to CCD cameras.[82] Optical lens systems have been used by many groups to provide an optical link for powder and single crystal screens and CCD cameras. A particularly effective scheme is to use one or more low depth of focus optical lens(es) combined with a single crystal scintillator.[45,80]

Before shifting the focus from apparatus to applications, it is worthwhile to consider some additional approaches available for optimising microtomography. Fan beam and cone beam apparatus generally employ point X-ray sources, and this allows geometrical magnification to match desired sample voxel size to detector pixel size (Fig. 1). The incorporation of time delay integration (mechanically coupled scanning

Table 1   Some CCDs used in microtomography

CCD type	Format*	Pixel size, μm^2	Dynamic range	Ref.
Thomson CSF TH78882CDA	384 × 576	23 × 23	5 × 10^4	80
Texas Instruments 4849	390 × 584	22 × 22	5 × 10^4	80
Kodak KAF-1400	1320 × 1035	6·8 × 6·8	4 × 10^3	80
Thomson	1024 × 1024	19 × 19	2 × 10^4	81
Loral Aerospace	1024 × 1024	15 × 15	4 × 10^3	81
Tektronix	2048 × 2048	24 × 24	8 × 10^3	81
EEV CCD02-06	385 × 578	22 × 22	…	82
Kodak	2048 × 2048	…	…	45

*Manufacture of 4K × 4K CCDs has also been reported.

of sample and detector) into a microtomography system[82] has allowed reconstruction of specimens larger than the CCD image area or the X-ray beam; directional correlation of noise in large aspect ratio samples remains a problem since this introduces streak artefacts.[88] Time delay integration has been quite successful in eliminating ring artefacts caused by non-uniform response of the individual detector elements.[82] Use of an asymmetrically-cut crystal, positioned between sample and X-ray area detector and set to diffract the monochromatic synchrotron radiation incident on the sample, has been demonstrated to reject scatter and improve sensitivity as well as to provide, through beam spreading, magnification of the X-ray beam prior to its sampling by the X-ray detector.[32,33,89] This is an adaptation of a commonly used method in X-ray diffraction topography that allows one to overcome limitations of the detector, i.e. to approach resolutions inherent to the X-ray source.

Materials applications

Microtomography has been applied to imaging inorganic composites and their response to deformation, to studying the naturally occurring composite of calcified tissues, to studying pathways for material transport in porous solids, and to studying fatigue crack closure in metal samples. The following four subsections summarise results in these four areas. There is some redundancy in the citations as the same data appear in very different contexts: review papers focusing on technique as well as publications focusing on materials science. The reader should also note that some studies such as the chemical vapour infiltration of SiC preforms span more than one area. Porosity in welds,[89] uniformity of laser fusion microballoons,[24] the fracture of bonding layers between ceramic plates,[90] carbon fibre based composites,[72,74] polymerisation particles,[70] catalyst distribution in polymer particles,[71] electronic components,[38,91] and microstructure in insects[27,92,93] have also been studied but will not be covered here in order to keep the review's length manageable.

Inorganic matrix composites

The field of inorganic composites is vast, and wide scope exists for applications of X-ray microtomography to processing and to damage accumulation and fracture of these composites. Both ceramic matrix and metal matrix composites have been studied by microtomography, including samples reinforced with continuous and discontinuous second phases. Particulates, chopped fibre, continuous fibre, and monofilament reinforced composites have all been examined.

In ceramic matrix composites, the reinforcements provide increased toughness and damage tolerance and are normally in the form of fibres. One strategy is to use the fibres to absorb energy by causing a network of microcracks to form, energy which might otherwise contribute to catastrophic propagation of a single, main crack. A second strategy is to use the fibres to bridge cracks which constrains the amount the crack can open and how far the crack tip can

extend. In virtually all ceramic matrix composites being considered for commercial use, both reinforcements and matrix have negligible ductility; therefore, the faces of microcracks and large cracks tend to resume contact once applied loads decrease to zero. Even with load applied, crack openings typically remain below a few micrometres; being able to detect such small features has been the main impediment to applying microtomography to quantification of damage in ceramic matrix composites and the reason why microtomography studies to date have focused on processing.

The pore structure in degassed and non-degassed reaction bonded, silicon nitride/silicon carbide was studied with 10 μm reconstructions of the 1 mm × 1 mm cross-section,[60] and the 15 μm dia. Nicalon fibres could not be resolved. The structure of channels between cloth layers in SiC–SiC composites has been also studied as has the densification of these composites by chemical vapour infiltration,[94–97] but discussion of these very interesting results is postponed until the third subsection. Images of a SiC monofilament–Si_3N_4 (91 wt-%Si_3N_4, 6%Y_2O_3, 3%Al_2O_3) composite have been obtained with microtomography;[98] in 111 μm thick slices, the 140 μm dia. fibres and their 30 μm dia. cores are quite visible, and the radial variation of linear attenuation coefficient at 24.0 keV for the SiC fibres agrees with others' 21 keV measurements of similar fibres.[99] Thermomechanical fatigue of ceramic as well as metal matrix composites has also been investigated.[100]

Before discussing metal composites results, consider the requirements for reliably detecting cracks with very small openings, say 0.5 μm. Assuming such a crack extends across the entire voxel and that the signal/noise ratio in the reconstruction is adequate for detection of one-quarter voxel of empty space, projections of the object must be recorded with 2.5 μm spatial resolution in order for the sample to be reconstructed with the required voxel size for crack detection. If a $2K \times 2K$ detector array were used, sample diameters up to 5 mm could be studied successfully. It is important to emphasise that detecting a crack 0.5 μm thick in a sample 5 mm thick requires sensitivity to changes in sample thickness of $\sim 10^{-4}$. On the one hand, cracks consist of spatially correlated voxels for low absorption, so this helps in detecting such narrow cracks. On the other hand, cracks often follow the interface between reinforcement and matrix, and this hinders detection.

Reports of microtomography of metal matrix composites appear to be limited to aluminum and titanium matrixes and have mostly focused on SiC monofilament reinforced composites,[43,60–62,72,76,98–106] not only because these composites offer important performance gains over other composites but also because the size of the fibres allows unambiguous identification of damage modes at individual fibres and because these results can be linked to work on damage mode characterisation in optically transparent glass composites employing the same monofilaments. Nonetheless, metal matrix composites reinforced with short, small diameter fibres[80] and with particulates[66,106] have

been studied; the latter study followed damage accumulation.

A pencil beam microtomography system was used to investigate several aspects of ceramic particulate reinforced aluminum composites.[66] Within a given cross-section of the powder processed composite, the content of 12 µm TiB$_2$ particles was found to deviate substantially from the nominal 20 vol.-% of reinforcement: contents as low as 10 vol.-% were reported. The local void volume fraction within the necked regions of a set of composite samples with 5, 10, and 20 vol.-% 30 µm SiC particles was also measured as a function of true strain. These types of measurement focus attention on the portion of the sample where damage is concentrated, offer a very sensitive probe of damage, and allow the same volume to be interrogated in three-dimensions multiple times during its evolution. Unfortunately, the sections were not completely contiguous, a limitation imposed by the quite low data acquisition rates with pencil beam systems.

A parallel beam system employing synchrotron X-radiation has been used to image aluminum matrix composites reinforced by Al$_2$O$_3$ whiskers 2–4 µm dia. and 50–80 µm length, or by Al$_2$O$_3$ fibres about 20 µm dia.[80] The sample diameter of the former composite was ∼1 mm while that of the latter, which was not reported, was apparently much less than 1 mm. The whisker reinforced composite is a material normally used for diesel engine pistons, and its aluminium matrix contains significant levels of Si, Cu, Ni, and Fe. The resulting intermetallic phases were seen to form a three-dimensional network whose mesh size was of the order of 15 µm. These investigations also found that the individual Al$_2$O$_3$ fibre images and the distribution of fibre images for the second composite agreed with scanning electron micrographs and demonstrated spatial resolution of 6 µm in the reconstructions (MTF of 80 line pairs mm^{-1} at 20% contrast).[80]

Microtomography of SiC monofilament–Ti matrix composites presents a somewhat different challenge than imaging small diameter particulate or chopped fibre Al matrix composites, or, for that matter, imaging the same monofilament in an Al matrix. While there is relatively little contrast between Al and SiC (their linear attenuation coefficients are quite similar),[99] the large absorption of Ti makes it difficult to detect changes within the SiC or C portions of the monofilaments.[102] Matrixes of Ti$_3$Al and Ti–6–4 (6%Al, 4%V) with Textron SCS-6 SiC monofilament reinforcements have been imaged using tube generated[72] or synchrotron X-radiation.[102] In these three- and eight ply, aligned fibre composites, matrix cracks and broken fibres could be clearly seen.

The bulk of the microtomography work on monofilament reinforced composites, however, has been on Al matrix materials and includes at least one PhD thesis.[104] With the exception of one damaged*,[107] sample of [0$_2$/±45]$_s$ eight ply SCS-2 SiC/Al,[102] the samples examined have consisted of aligned monofilaments. Figure 4 shows the radial variation of
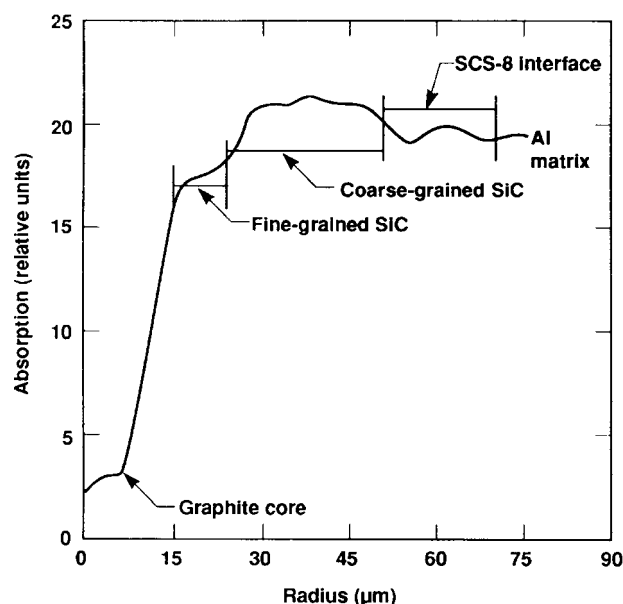
4 Radial variation of absorption for 140 µm dia. SiC monofilament.[99,104] © Materials Research Society

absorption measured for the SiC fibres and identifies the different microstructural zones of the fibres. The 32 µm dia. graphite fibre cores are distinct, even without averaging, and radial averaging over many slices and fibres was necessary to overcome the noise in the data and to reveal the several regions of somewhat different compositions[99] consistent with reported variations of stoichiometry.[108,109]

In an eight ply, as processed SCS-8 SiC/6061-0 Al matrix composite (Fig. 5), considerable intra-ply, processing related porosity was noted in reconstructions.[60,99,101,104] Monochromatic synchrotron X-radiation with energy between 20 and 22 keV was used to collect the data for these reconstructions with 6 µm isotropic voxels. The contrast between SiC and Al is quite small at these energies, so that porosity and the monofilaments' carbon cores are the most visible features, and differentiating between fibre cores and porosity requires careful scrutiny and a close eye for the weak contrast between SiC and Al. As an aid to the eye, the SiC/Al boundary of one fibre in Fig. 5a is traced with a dark circle, and an arrow points to a matrix pore. Based on examination of many slices, loading to 828 MPa and beyond eliminates much of the porosity (compare Fig. 5a and b). Likewise, measurement of the separation between fibre cores of first and higher order neighbours reveals that the fibre centres become more regularly spaced as the load increases. The slice in Fig. 5b was close to the fracture surface, and fibre fracture as well as fibre–matrix disbonds are seen. Thus, as monotonic load increased, the porosity disappeared and fibre spacing became more regular.[101] It is doubtful whether fibre rearrangement and porosity elimination would have been uncovered in studies of polished sections: too much labour would be required to interrogate enough serial sections.

Reconstructions with isotropic 6–7 µm voxels of ∼1·5 mm × ∼1·5 mm cross-sections cut from coupons

*The sample (the outer two plies on each side of the sample were parallel to, and the four central plies were oriented at ±45° to the load axis) experienced 5·0 × 10^6 cycles with $R = \sigma_{min}/\sigma_{max} = 0·3$ and load range of 413 MPa.[107]
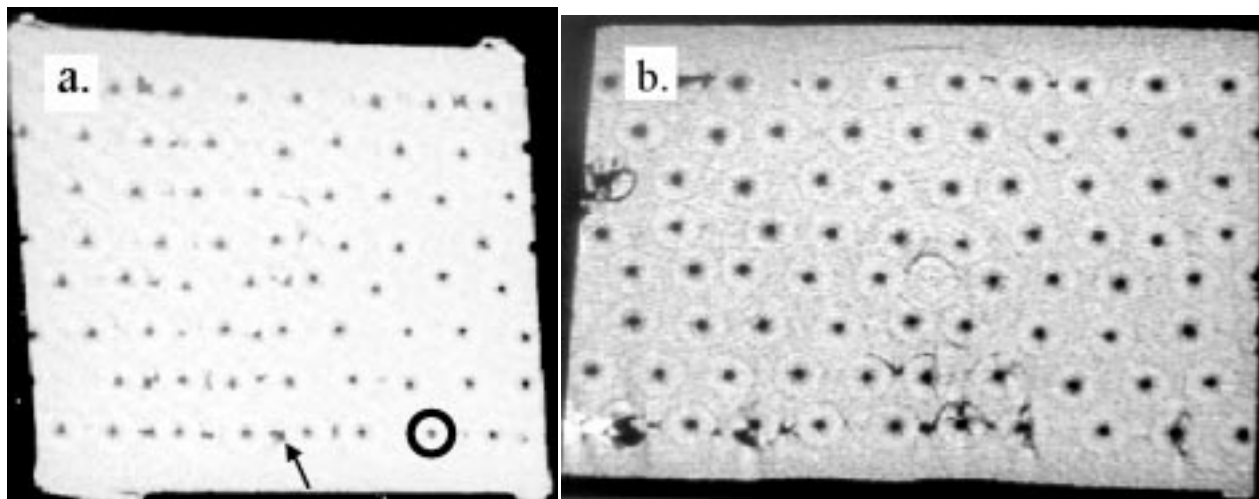
5 Slices perpendicular to SiC monofilament fibres in *a* as received state and *b* after loading to 1448 MPa (failure). The darker the pixel, the lower the X-ray attenuation. Eight plies lie horizontally, and top and bottom of each image (surfaces of composite plate) are 2·5 mm apart. In *a* SiC/Al interface of single fibre is traced with circle and arrow points to matrix pore.[101,104] © Materials Research Society

of the same composite panel reveals that observation of increased mechanical stiffness after the first few fatigue cycles corresponds to elimination of the processing related matrix porosity (initially 2–7 vol.-%) and to displacement of the fibres from somewhat irregular arrangement into a more nearly hexagonal array (similar to Fig. 5).[99,102] This study showed the fibres rearranged and the porosity disappeared by the time the load reached 828 MPa. Fracture of the C cores of the SiC fibres appeared to occur before 828 MPa and to nucleate the subsequent SiC fracture, but SiC cracking could not be observed except after fracture ($\sigma = 1448$ MPa), no doubt because the cracks are pulled closed by the relaxation of adjacent fibres at lower stresses. In fractured samples of this metal matrix composite, however, spiral and planar cracks within SiC fibres can be seen quite clearly with microtomography:[45,104] Fig. 6 includes only the low absorption voxels from within the volume containing a single SiC fibre. The carbon core extends vertically to the sample surface (top) where the fibre pulled out of the matrix. The observation of C core fracture in the SiC fibres illustrates one of the advantages of tomography: this observation could not be made with serial sectioning and optical or scanning electron microscopy since any such fractures observed would undoubtedly be attributed to polishing damage.

Crack detectability has also been studied in Al–SiC monofilament composites using a thin wedge pushed into a sample parallel to the fibre axes.[61,62] Two orientations of the wedge were examined, perpendicular to the eight plies of the composite and 45° to the plies. A pencil beam system with a 10 μm dia. collimator, a Pd filter, and an energy sensitive detector set for Ag K_α radiation allowed slices perpendicular to the monofilament axes to be reconstructed with 12·5 μm isotropic voxels. Crack opening displacement in the plane of the plies was measured as a function of distance from the tip of the wedge by direct measurement of the opening or by comparing the separation of fibres on either side of the crack with

that of the same monofilaments in the first slice beyond the tip of the crack. Results of the two measurement techniques agreed within 2 μm (within about 15% of 1 voxel). The wedge at 45° to the plies was inserted 2·1 mm into the $\sim 1{\cdot}5$ mm $\times \sim 1{\cdot}5$ mm sample, which was not far enough to cause significant fibre fracture, but it did cause significant fibre displacement, fibre–matrix debonding, and ductile rupture of the Al matrix. The wedge perpendicular to the plies caused substantial fibre fracture. Cracks open as little as 1–2 μm, i.e. 10% of a voxel's width, could be detected. Opening as a function of distance from the wedge tip was very different for the two geometries and reflected whether or not fibre fracture had occurred. With the 45° wedge, opening decreased fairly uniformly and quite rapidly until about 700 μm from the tip of the wedge, whereas with the 90° wedge, opening was roughly constant and much larger (than that in the 45° sample) between 100 and 1000 μm from the wedge tip after which the crack became invisible within 100 μm.

The relatively well behaved gradients in crack opening produced in the studies cited above allowed detailed assessment of how well crack opening can be quantified for a given level of noise in the reconstructed images. Besides controlling the amount of opening allowed, the fibres provided a built in fiducial for measuring crack opening: the change in fibre–fibre separations. In other words, the difference in two monofilament's separation across the crack at a particular position and that far from the crack tip should give an accurate measure of opening at the position in question. Most samples in which crack opening needs to be measured do not have these fiducials, so that crack opening must be quantified by summing the openings in adjacent partially open voxels. It is difficult to trust the robustness of such a procedure without at least once checking its results against those of a fiducial based opening measurement; thus, the results of the wedge studies offer important guidance not only for how small an increment of crack opening can be quantified in

monolithic samples but also for detection limits (in terms of partial voxels) for other high contrast features.

Three point bending of a notched eight ply SiC–Al monofilament composite has been studied with a pencil beam system[60] and a CCD system[101] and summarised in Ref. 104. Broken fibres, matrix cracking, and fibre–matrix disbonds were observed. The notch was 0·6 mm deep and ~0·8 mm wide, and it was on the tensile side of the 1·5 mm × 1·5 mm cross-section of the sample. Outside the notch only a small amount of fibre disbonding was present adjacent to the end of the notch. Most of the damage was confined to within the material ahead of the notch. Large lengths of fibres had pulled from the matrix, and the authors noted that the matrix–fibre shear zone extended 200–300 µm beyond both ends of fractured fibres. The fibre fracture surfaces were not planar, and significant plastic deformation was inferred to have occurred after fibre fracture and pullout.

In addition to the monotonic and fatigue damage study of SiC–Al cited above,[104] *in situ* observation of monotonic deformation in an Al–SiC monofilament composite has also been reported.[105] In this latter study, the 140 µm dia. fibres were cut into 1 mm lengths and included in a 1 mm dia. sample at a volume fraction of 0·10. These dimensions are rather unrealistic when compared to typical monofilament reinforced composites, but it appears that they were convenient for microtomography and, in the case of the monofilament length, avoided the need to apply large loads and avoided unstable fracture once the ultimate tensile stress was exceeded. Observations were reported at zero stress, at a stress just before failure, and after the sample failed. An X-ray pickup tube was used with 23 keV synchrotron radiation; unfortunately the two-dimensional detector could be used to record only a maximum of 40 slice planes due to computer memory limitations. The slice width and interval between slices were 31 and 79 µm, respectively. Despite the difficulty of working with a set of non-contiguous slices and the decreased crack sensitivity due to the relatively large slice thickness, the authors report fibre–matrix disbonding, fibre pullout, and matrix cracking only at the maximum stress (and, of course, in the failed condition). From observation of the failed composite, the authors inferred that the matrix crack observed at the maximum stress propagated close to several monofilament segments and led to the sample's failure. Because of the small monofilament lengths, the relatively low volume fraction of reinforcement and the relatively small sample diameter (compared to the monofilament diameter), it is unclear whether the conclusions represent what occurs during fracture of composites containing the much longer monofilaments typically employed.

The reconstructed images of composites cited above suffer from a large amount of noise relative to the difference in absorptivity between the Al matrix and the SiC fibres. Improving the signal/noise ratio in the reconstructions requires much longer counting times: most investigators agree that decreasing noise in reconstructions by a factor of 2 increases data collection time by 2^3, but detector elements can collect only a finite number of 'photons' before becoming

saturated. Because the incident beam must cover the sample entirely, some detector elements invariably see the unattenuated direct beam, and the time required to saturate these elements represents the maximum counting time for a view. Less noisy reconstructions might be obtained by collecting many views along the same projection direction and adding them together point by point to extend the dynamic range of the collected data, but this has not been investigated extensively and beam instabilities can become important if the averaging time becomes too long. The particular application and sample geometry dictate whether extraordinary measures are required.

The rapid change of attenuation coefficients across most interfaces poses a particular challenge for accurate reconstruction. This is a greater problem for SiC reinforcements in a Ti matrix than in an Al matrix, for example, and an experimenter's choice of X-ray energy needs to consider the desired difference in contrast between reinforcement and matrix as well as optimum sample transmissivity. There is a large area of internal interfaces, and detecting cracking at these interfaces, an important failure mode, presents a very real challenge. Little can be done if the interface cracks are tightly closed, except if *in situ* loading can be applied to open the cracks. Even when these cracks are open, it is difficult to detect the change of attenuation from the crack superimposed on the transition in absorption across the interface. Considerable caution must be exercised, therefore, in quantification of interface cracking using X-ray microtomographic reconstructions.

Transport in porous materials

Understanding the role of porosity, in particular the pore connectivity, in material transport is crucial in fields as diverse as oil production, filter operation, and composite material densification, and published reports of computed tomography in all three areas have appeared.[94–97,110–117] Transport is, of course, important in biological structures (e.g. trabeculae in cancellous bone, Haversian canals in cortical bone, and blood vessels in other organs), but this discussion is postponed until the following section.

A priori microstructural knowledge could aid in design of a drilling fluid that would cause minimal formation damage from particle invasion[113] for example, or composite preform architecture or infiltration conditions could be altered to provide more uniform and complete densification. Representative volumes of highly variable structures such as geological core samples and ceramic cloth preforms have been studied with microtomography. In addition to the focus on pore topology, assessing how well different phases could be detected has received more attention. Pencil beam, cone beam, and synchrotron parallel beam microtomography systems have been used to study Fontainebleau and Berea sandstones, a Texas creme chalk, and glass bead packs.

A Fountainebleau sandstone (porosity fraction = 0·197 and experimentally measured permeability $K_{exp} = 1860$ mD, where 1 Darcy = 10^{-12} m^2 and the permeability relates the volumetric flow rate divided by the cross-sectional area to the pressure gradient
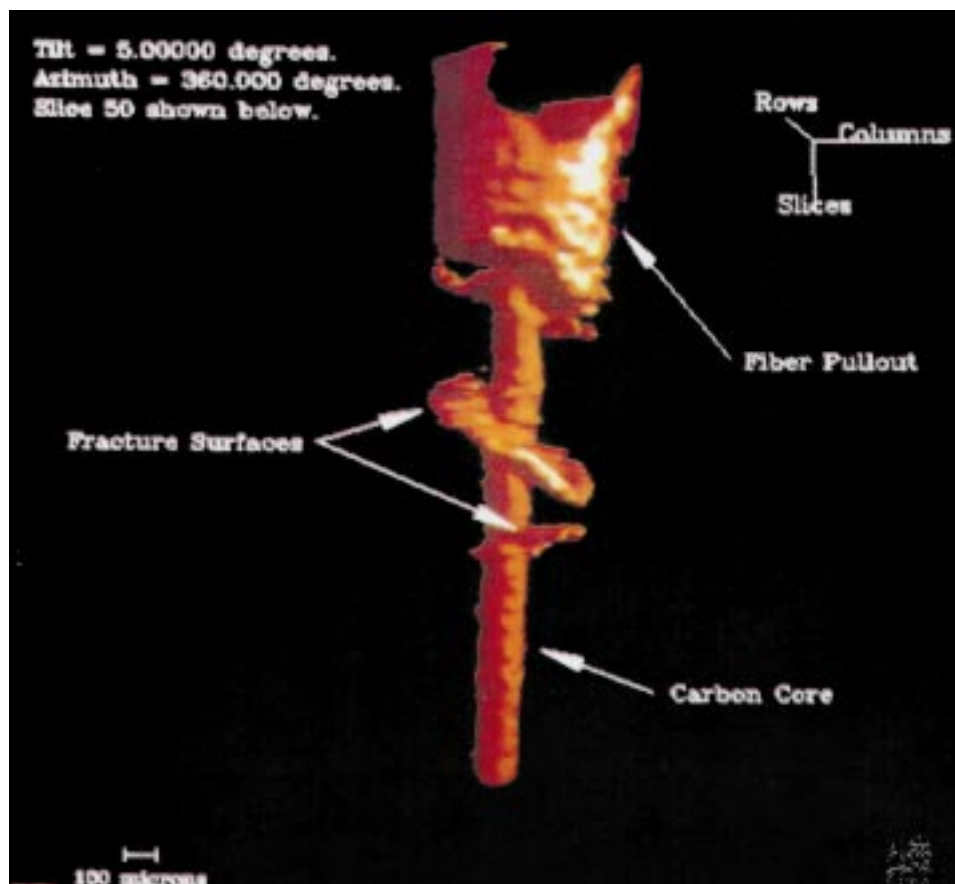
6 Three-dimensional rendering showing surface of low absorption voxels within SiC monofilament in fractured Al–SiC composite sample. Fracture surface is at top, and graphite core C extends down from fracture surface. Large diameter cylinder atop carbon core shows where SiC monofilament pulled from Al matrix in this half of sample. Midway down fibre a spiral crack in SiC is visible[45,104]

divided by the Newtonian viscosity) was studied with a 5 μm × 5 μm dia. beam of ∼19 keV photons. An image matrix of 303 × 303 10 μm × 10 μm elements was formed for 100 slices separated by 10 μm.[113] The permeability calculated for the imaged sample agreed with that measured directly in larger samples. A second study of Fontainebleau sandstone[114] examined 3·5 mm dia. samples with a synchrotron CCD based system and imaged three samples with isotropic 7·5 μm voxels and image cubes of 288 × 288 × ∼235 voxels. In this second example, the authors note that the samples contained about seven grains on a side, which is close to the minimum size to estimate permeability with accuracy, and calculated permeabilities from the microstructure of 1000–1300 mD, in good agreement with experimental values determined with several other techniques. Since Fontainebleau sandstones are reported to be remarkably homogeneous for geological materials, the agreement between these two studies is not surprising. Modelling of fluid permeability in both studies showed large variability in fluid flow depending on which subset of the reconstructed volumes was used to define the three-dimensional channel structure. Because several different numerical methods were used, it appears unlikely that the variability can be due to anything other than changes in channel architecture. This demonstrates on the one hand how powerful microtomography imaging can be in

determining *local* transport conditions and on the other how much care must be taken to ensure representative volumes are imaged and to avoid over interpretation of limited data.

Microtomogrphy results from three Berea sandstones, a Texas creme chalk and a glass bead sphere pack have also been reported;[113] the sample dimensions (2·5 mm in each direction) and the reconstruction meshes (303 × 303 × 250 with 10 μm spacing) were similar to those in the studies cited above. The air permeabilities of the geological samples ranged over nearly three orders of magnitude (from 1000 to 16 mD), and the results confirmed that pore structures could be followed in materials representative of those found in petroleum reservoirs. When the glass bead pack was infiltrated with a mixture of oil and water, the authors found their results were clear enough to allow at least three fluid phases to be resolved. The ability to resolve oil from water or other phases is important in understanding how, during secondary recovery, some oil being swept by the driving fluid becomes immobilised by capillary forces and forms isolated, unextractable blobs. Others have compared the distribution of various fluids in porous geological material (determined by microtomography) with magnetic resonance relaxation times[111] so as to enable rapid, non-imaging characterisation.

Similar pore topology exists in ceramic matrix composites partially densified by chemical vapour

infiltration (CVI).[94–97,110,111] The goal with ceramic composites is to maximise the density produced by processing so that the toughening effect of the reinforcement is fully realised; an evolving structure must be understood in this case. Production of complex, near net shape parts results for materials which are very difficult to machine; cost savings for SiC–SiC composites can be enormous. The preforms of these composites are often constructed by laying layers of cloth to form the required thickness or by wrapping multiple layers of cloth around a mandrel. In CVI, the preform is infiltrated by a vapour precursor which decomposes and deposits the desired phase within the composite. Another approach, reaction sintering, fills the preform with a very fine powder and forms the matrix by reacting the precursor with a gas. While reaction sintered samples have been studied with microtomography for different processing conditions,[59] the principle work has been in CVI of SiC–SiC composites.

Use of a portable reaction chamber allowed Nicalon (amorphous SiC, Nippon carbon)–SiC composites to be transported to a synchrotron radiation source between increments of CVI and to be imaged multiple times with microtomography.[94–97] The graphite chambers were cylindrical with a 10 mm outside diameter, and the Nicalon cloth preforms, each 6·2 mm dia. and 6·0 mm high, consisted of 20 layers stacked within a chamber. Each cloth was woven of bundles or tows of ~500, 10–20 μm dia. Nicalon fibres, and there were approximately 6·3 tows cm^{-1}. Two architectures were examined: 0/90° layups, where the tows in adjacent cloth layers are parallel, and 0/45° where the tows in adjacent layers are rotated 45°. The preforms were infiltrated with methyltrichlorosilane (MTS) at 975°C, and the MTS flow was adjusted so that after 3, 6, and 9 h densification would be 33, 67, and 100% complete respectively.

Samples were imaged prior to and after each increment of CVI, 400 contiguous slices were recorded and the reconstructions consisted of isotropic 15·8 μm voxels. Data could not be collected at high resolution because of the need to keep the entire reaction chamber in the field of view, i.e. as a direct consequence of the number of elements in the CCD detector. In the 0/90° preform, the structure of the channels between cloths depended on the relative displacement of the holes in the cloths bounding the channel,[94–97] and this relationship is illustrated in Fig. 7. Offsets 45° to the two axes resulted in very closed channels (Fig. 7, top), hole displacements along the two directions produced an array of parallel, one-dimensional open pipes (Fig. 7, middle), and when the holes were aligned, a two-dimensional network of openings was observed in the channels (Fig. 7, bottom).

A consequence of the voxel size was that individual micropores within the tows could not be resolved, even in the preforms. Nonetheless, accurate volume fractions of Nicalon, deposited SiC, and miropores were obtained by taking averages over several subvolumes within tows for preform and for 3 and 6 h infiltration.[94,95] Comparison of a microtomographic section through a densified Nicalon–SiC composite with an optical micrograph of nearly the same section
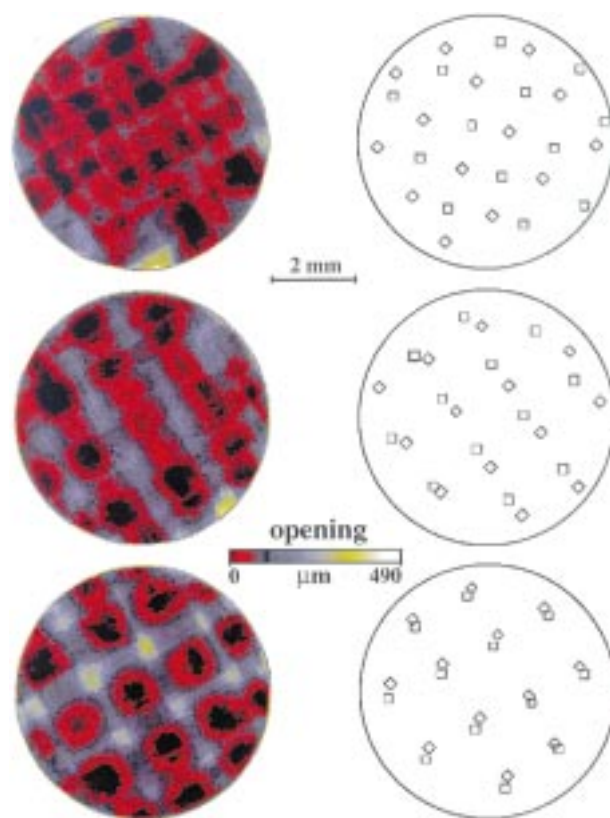
7 Maps of three patterns of channel width (left column) as function of relative positions of holes (squares and diamonds) in plane weave Nicalon cloths on either side of each channel (right column). Black pixels show positions of lowest opening, with red, blue, green, and white showing increasing opening. (Top) Poorly defined, relatively closed channel due to hole displacements 45° to tow direction. (Middle) Hole displacements along tow direction and set of parallel, one-dimensional channels. (Bottom) Closely aligned holes and resulting two-dimensional network of openings.[94–97] © Materials Research Society

demonstrated the accuracy of the reconstruction.[45] Measurement of surface area per unit volume as a function of fractional density[94,95] agreed well with the uniform deposition model used to describe the CVI process;[118] the slight differences could be attributed to the fact that the surface area per unit volume of macroporosity (channels and holes through cloth layers) could be measured and the measurements could not include microporosity.

Materials transport is also important in solids which do not have well defined porosity, and, while it is difficult to see how microtomography could become a universally applied tool in this context, it has been shown to be very effective for non-destructively quantifying the spatial distribution of corrosion products within printed wiring boards.[63,91] In the presence of high voltage gradients, copper can diffuse and form conductive anodic filaments (CAF) and short out circuit elements,[119] and microtomography has been used to quantify the amount of copper within CAF. Results of microtomography[63] were in excellent agreement with serial sectioning and the amount of copper

removed from the copper anode. It is important to emphasise that the copper halide deposits comprising the CAF are typically 20–40 μm below the surface of the printed wiring board, that the translucent boards allow only indistinct visualisation of the CAF with optical microscopy, and that an X-ray method is required for non-destructive characterisation. Because the contrast from the printed wiring board is so variable and the contrast of the CAF along any particular viewing direction is so weak, radiography cannot provide images better than those from optical microscopy. This work demonstrated how subsurface CAF formation kinetics could be deduced non-destructively with microtomography.

Calcified tissue

Numerous microtomographic studies of bone and teeth have appeared and are likely to continue to appear on a regular or even accelerating basis. Concerns such as osteoporosis and bone fracture in the elderly contribute to this activity. The normal biological variability between individuals and the fact that the calcified tissue is alive and alters its structure in response to stimuli makes studies of calcified tissue more involved than those discussed above. Obtaining statistically representative measurements of volumes of material is a particular advantage of microtomography. In a limited number of cases non-destructive, *in vivo* comparisons of the same tissue volume have been possible. For example, entire rats and mice can be imaged *in vivo*,[34,35] direct comparisons have been made of the bone before and after induction of oestrogen depletion and onset of the accompanying osteoporosis,[120] and imaging with X-ray energies above and below the Xe K edge allowed very sensitive mapping of the distribution of fat (which absorbs Xe heavily) within the head of a rat.[73] Interconnection of trabeculae (individual small plates or struts of calcified tissue which form a meshwork in spongy bone) can be followed with serial sectioning and image analysis,[121] but microtomography has proved to be an efficient alternative without requiring specialised sample preparation.[122] Interconnected Haversian canals in cortical bone (channels for blood vessel and nerve supply for the surrounding dense bone) and coronary arteries in rat hearts and kidneys are other examples.[123] Comparing results of microtomography with histological sections[93,122,124] and with results from other modalities[125–127] has been very valuable. The review of Davis and Wong[67] provides a good introduction of what has been done prior to 1996.

The most natural way of discussing studies of calcified tissue is to focus on the type of mineralisation. On the one hand are cortical bone and teeth which have relatively uniform mineral distribution while on the other is cancellous bone consisting of a lattice of plate-like trabeculae and rather anisotropic mineralisation. Emphasis is typically on the degree of mineralisation for the former and on dimensions and three-dimensional structural arrangement of the trabeculae for the latter. Various relatively large organs have also been imaged,[22,68,128] but these proof of principle studies fall outside the scope of a discussion of X-ray microtomography.

Teeth consist of an outer covering of enamel and an internal hard tissue dentin. By measuring the linear attenuation coefficients of enamel and dentin, Elliott *et al.*[129] appear to have been the first to quantify the difference in mineral content. Wong *et al.*[130] demonstrated that a molar and developing incisor could be distinguished quantitatively within a mouse mandible. Gradients in mineral concentration in enamel but not in dentin were found from apex to incisal end of a lower rat incisor.[131,132] Elliott *et al.*[133] and Kinney *et al.*[134] studied demineralisation at a carious lesion and subsequent remineralisation at the same site. Deciduous enamel defects in low birthweight children have been easily distinguished from normal regions in the same teeth.[127] Mercer and Anderson[135] report effects of applying CO_2 laser pulses to human enamel. The ability of microtomography to quantify microstructure repeatedly can be key to following processes in biological structures whose microstructure varies greatly between individuals.

Nielsen *et al.*[136] provided a three-dimensional rendering of the root canal in an endodontically prepared human maxillary molar, and the tissue loss (i.e. increase in volume of the root canal space) due to the endodontic procedure was clear even in the 127 μm × 127 μm pixels of the reconstructions. Dowker *et al.*[137] obtained similar images of human upper third molar, upper central incisor, and upper lateral incisor with and without files inserted in the root canal; these data consisted of isotropic ∼39 μm voxels and showed considerable detail such as unfilled space in the canal sealant and the presence of dentin debris (Fig. 8). Dowker *et al.*[137] also indicated that the three-dimensional data sets will be used to illustrate the variety of complexity of root canals during computer assisted dental training. It is interesting to contemplate whether X-ray microtomography of engineering materials can provide analogous computer assisted learning opportunities for undergraduate and graduate engineering or science students. Future microtomography applications are expected to include imaging accessory canals and investigating fluid transport into root filled teeth; one anticipates improvements in clinical procedures will soon be a direct consequence.

Cortical bone has been studied by numerous investigators but much of the work has focused on demonstrating what microtomography can see. Images of a human finger bone, for example, have been obtained at various X-ray energies in a demonstration of dual energy microtomography.[28] Infiltration of a KI solution into a section of deer antler[67] was also observed with a dual energy technique, but using tube generated X-rays. The cortices of rabbit tibia have been imaged and the results appear to indicate little, if any, change in mineralisation levels across the bone.[122,138] Cortical bone from human femora have been imaged,[51–58,82] and Haversian and Volkmann canals (for blood supply and innervation axial and transverse to the femur axis respectively) have been resolved. Rat femora have been the subject of considerable quantitative work, including microtomographic calibration of back scattered electron microscopy (BSEM) mean atomic number images,[139] comparison of microtomography data with fluorescence data in a study of
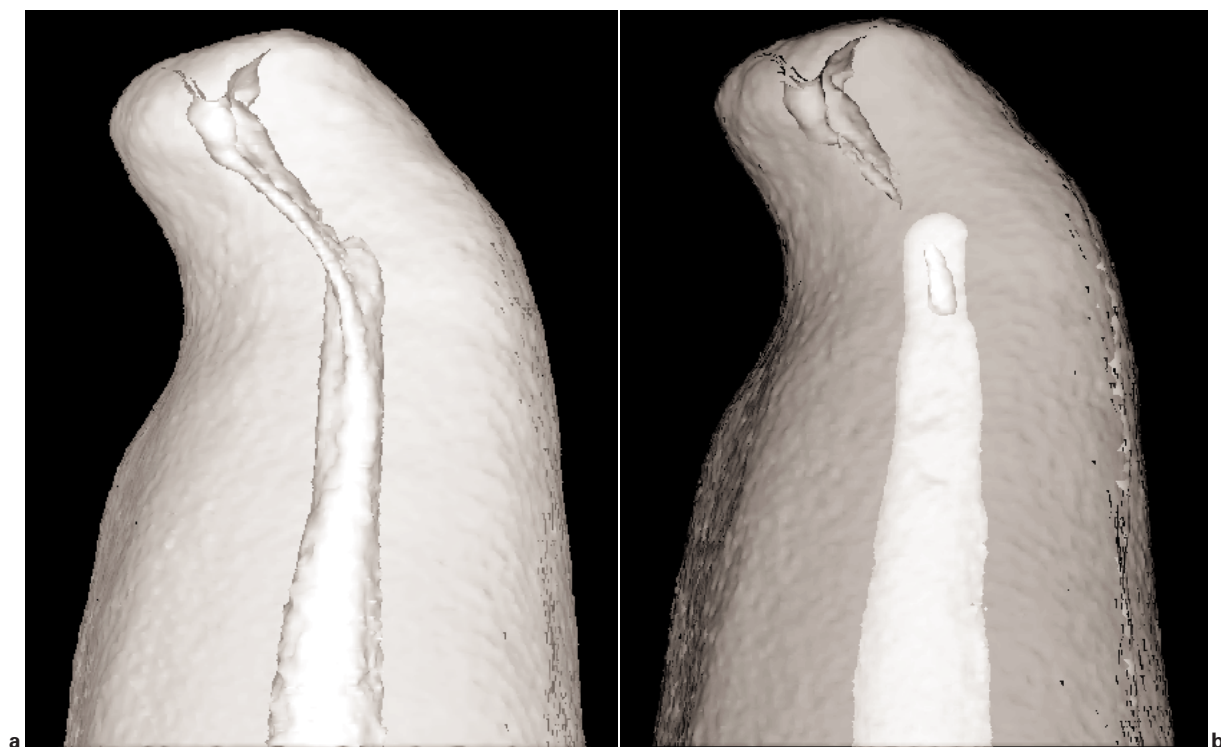
8 Surface renderings of upper lateral incisor after completion of root canal procedure showing both inner and outer surfaces. Tooth after completion of filing of *a* root canal and *b* tooth after filling canal with sealant (white pixels in tooth centre); surface of porosity remaining within sealant is superimposed on rendering of sealant. Reproduced with permission of Mosby, Inc. from Ref. 137

aging bone,[125] and the effect on mineralisation of space flight;[140] and the mineral content of the youngest cortical bone in a rat femur was found to match that of young, metabolically active trabecular bone.

Spaceflight has a considerable effect on bone, and microtomography was used to map the distribution of mineral content as a function of distance from the head of femora of growing rats.[140] These authors identified 'striking regional differences' in the distribution of mineral associated with femur maturation, areas most vulnerable to mineralisation defect (i.e. failure of newly grown bone collagen to acquire mineral) and areas most likely to yield information on the role of collagen production in the defect formation.

The network of small plates or trabeculae constituting cancellous bone are quite fine, and higher resolution microtomography is required for quantitative analysis of these samples than for those of cortical bone or of teeth. In addition to absorption tomography, described below, trabecular bone has also been imaged with scattered radiation.[126] Trabeculae in microtomographic sections reconstructed with $\sim$26 μm voxels appear clearly within a $\sim$6 mm dia. biopsy from a human iliac crest.[65] A similar sized sample from a fractured hip was imaged with a pencil beam system at 25 μm spatial resolution; marrow was removed prior to imaging and the mineral content was consistent with osteoporosis.[69] The morphology revealed in these two sections is quite similar. Other studies have also imaged trabeculae.[12,141–153] The effect of spatial resolution on topological measurements has been emphasised,[151] and proper choice of

threshold is necessary to produce accurate three-dimensional renderings such as that shown in Fig. 9.

Earlier serial sectioning of cancellous bone and unbiased estimates of connectivity did not reveal a simple relationship between connectivity and bone volume fraction.[121] Using microtomography, Feldkamp *et al.*[142] investigated anisotropy and connectivity within 8 mm cubes of human cancellous bones. In another study, numerous 8 mm cubes of human cancellous bone (four cadavers without known bone disorders, various bones and cube orientations) were imaged with 50 μm isotropic voxels prior to mechanical determination of modulus and ultimate strength.[79,148] Bone volume fractions ranged from 6 to 36%, trabeculae thickness from 0·10 to 0·19 mm, and spacings from 0·32 to 1·67 mm. In normal bone, strong correlations were found between the independent structural measures of bone volume fraction, trabecular plate number, and connectivity, and strong relationships were found for modulus and ultimate strength, accounting for 80 to 90% of the variance in these properties. Other work on modelling elastic moduli, based on three-dimensional networks defined by microtomography, appear elsewhere.[147,150,152] Goulet *et al.*[79] suggest that mechanical influences seem to alter the amount of bone by changing trabecular thickness while hormonal and/or chemical influences act to affect the number of trabeculae; this view seems consistent with the results presented in the following three paragraphs as well as the literature cited by these authors. It is also almost certain that the correlations between experimentally measured macroscopic properties and modelling based on the
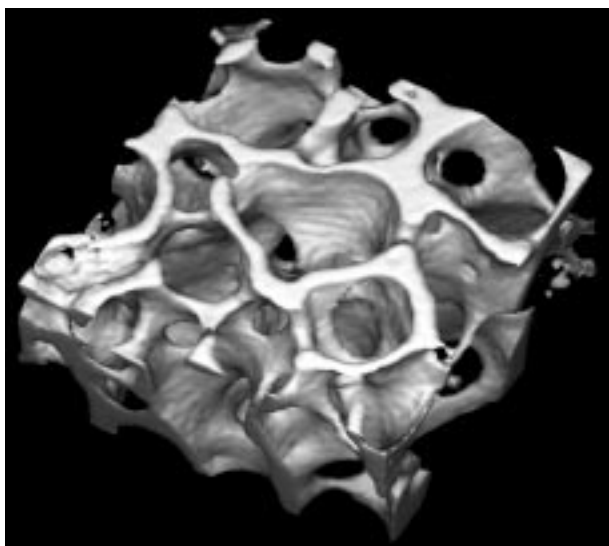
9   Three-dimensional rendering of 45 continuous slices of human bone biopsy from femoral head. Surface of ~2·7 mm × ~2·7 mm cross-section was defined with threshold of $3·0\ cm^{-1}$, and data were collected with Ag K_a radiation at 44 µm resolution. Reproduced with permission of IOP Publishing Ltd from Ref. 67
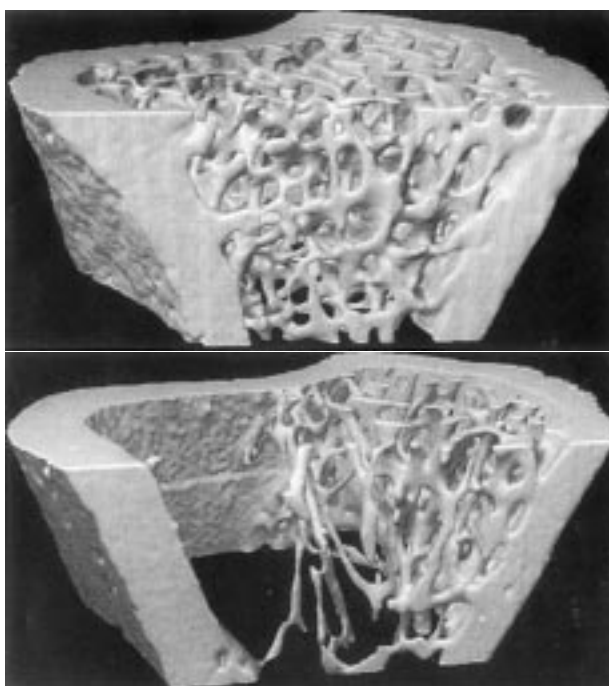
10   Three-dimensional visualisation of cortical and trabecular bone in proximal tibia of female rat imaged just prior to (top) and 5 weeks after (bottom) ovariectomy. *In vivo* imaging performed with 25 keV synchrotron X-radiation and covered volume approximately 1·5–3·5 mm distal to growth plate. 60% decrease in trabecular bone volume was observed, and much of remaining volume was in form of disconnected fragments. Reproduced with permission of the American Society for Bone and Mineral Research from Ref. 120
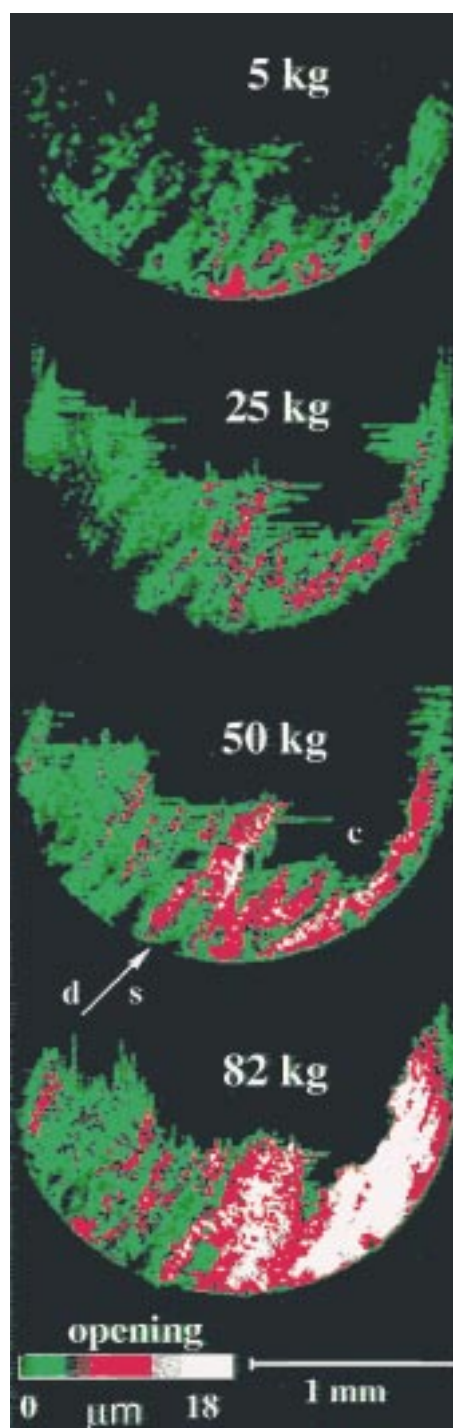
11   Map of fatigue crack opening in notched tensile sample of Al–Li 2090 T8E41 as function of applied load. Sample was reconstructed with ~6 µm isotropic voxels, and maps were produced by projecting openings on to plane perpendicular to loading axis. Loads at which sample was imaged were chosen to cover unloading portion of a fatigue cycle. White pixels show where openings were greater than 18 µm, red shows intermediate openings (on the order of 9 µm), and decreasingly smaller openings are shown as blue, green, or black respectively. © Elsevier Science Ltd and Acta Metallurgica Inc. (AMI), Ref. 168
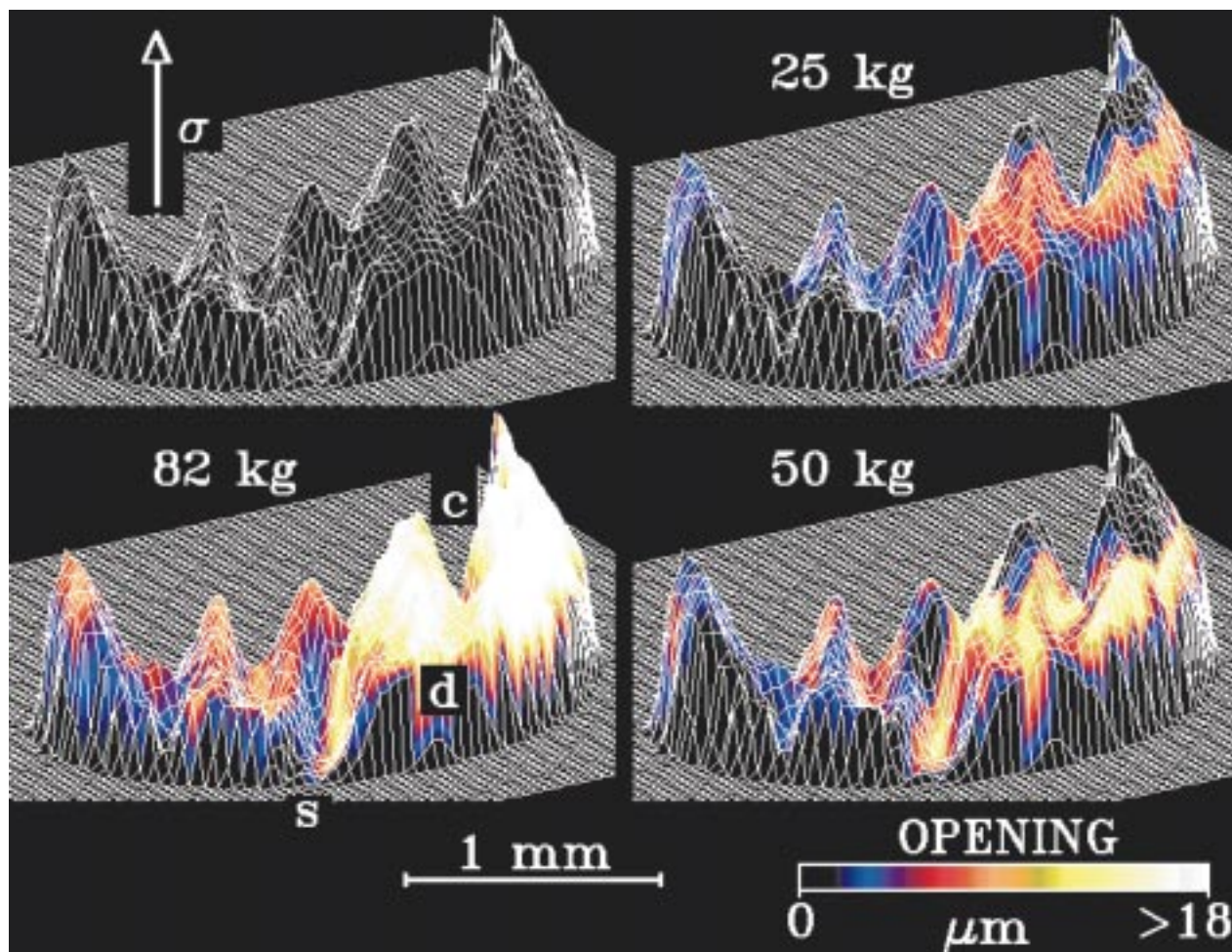
12 Mesh maps showing three-dimensional crack surface for notched tensile sample shown in Fig. 11. Only portions of sample containing crack are shown, and viewing perspective is from outside sample from side at which crack began to grow. Colours superimposed on three of the meshes indicate openings for each position, with white being greatest and yellow, orange, red, blue, and black indicating decreasing openings. Labels 'c', 'd', and 's' in lower left mesh mark same positions as in Fig. 11, and loads are indicated above each mesh. © Elsevier Science Ltd and Acta Metallurgica Inc. (AMI), Ref. 168

actual microstructure would not have been demonstrated without X-ray microtomography. In theory, one could measure elastic response and then use exhaustive serial sectioning to define the trabecular network for use in three-dimensional modelling; in practice, the labour required prohibits this approach.

Quantitative (conventional) X-ray computed tomography and dual energy absorptivity (i.e. quantitative radiography) have demonstrated that these density measurements of human femora explained no more than 30 to 40% of observed variance in modulus and 50 to 60% of the variance in ultimate stress, and that the orientation of cancellous cubes in the principal compressive trabeculae region was a significant contributor to mechanical properties independent of the bone density,[154] a direct indication that trabecular microstructure is important in bone strength. Changes in trabecular morphology (thickness, relative density, bone fraction, and separation) were studied in a guinea pig model[142,143] and in a canine model[114] of osteoarthritis; of particular interest in the canine study was that osteoarthritis was induced in one knee of the dog while the other knee was left unaffected and served as a control; earlier microtomography work

showed less than 5% differences in mean bone morphology variables between legs.[155] Kinney and coworkers[120,149] imaged (25 keV X-ray photons, other parameters of the reconstruction were not specified) trabecular bone architecture of rat tibia *in vivo* before and 5 weeks after ovariectomy induced osteoporosis and found a major loss in trabecular bone following ovariectomy (Fig. 10). More important was the change from an interconnected plate and strut-like structure to one that is mostly disconnected, dangling trabecular elements (a morphology not observed in non-ovariectomised rats). Finally, a strong linear relationship was observed between connectivity and volume of trabecular bone.

Bonse *et al.*[156] showed volume renderings of cancellous bone biopsies from a single patient over 15 years; the three-dimensional renderings clearly show the large loss of bone as a result of chronic hemodialysis from which the patient was suffering. Numerical values for the volume fraction of bone and the ratio of the bone surface area/bone volume are presented for the five biopsies shown. From these data, it is possible that the main change is in the number and connectivity of the trabeculae and not

in their thickness. Others have studied trabecular changes in pre- and post-menopausal women and numerically simulated changes in density and architecture beginning with the normal, pre-menopausal structure.[153] It is likely that these studies will multiply, given the aging populations in the industrial world. Further, a number of companies are marketing reasonably priced turnkey microtomography systems (that is, compared to the cost of a typical biomedical research project).

Healing processes have also been studied. Images of microcallus formations within trabecular bone have been interpreted to show the healing process after microfracture.[12] Guldberg and co-workers[157] inserted a small chamber into dogs' femora and tibia and observed tissue repair with microtomography and other methods after the 7 mm internal dia. chambers were removed from the animals. Repair response with and without mechanical stimulation was studied, and after 12 weeks the bone volume fraction was 75% larger in the loaded group relative to the unloaded control group. Trabecular connectivity was increased for the loaded bone relative to the control groups, the trabeculae were much thicker in the loaded biopsies but the trabecular spacing was the same as was the number of trabeculae. The results support the hypothesis that newly formed bone is deposited in mechanically appropriate locations, and Guldberg *et al.*[157] suggest that the limitation of strain magnitude is important in the process of tissue adaptation.

Fatigue crack closure

During fatigue crack propagation, application of a cyclically varying load drives crack extension, and many variables can affect crack growth rates. Processes such as fatigue crack closure, explained below, greatly alter crack propagation rates, and understanding these has been the focus of considerable research. X-ray microtomography with *in situ* loading of samples has recently been used to study how, at what stress/stress intensities, and where crack faces come into contact or separate during a fatigue cycle. After a brief description of the crack closure phenomenon, results obtained on an Al–Li alloy are discussed.

Fatigue crack closure describes situations where the crack faces come into contact prematurely during unloading of a sample (i.e. before the minimum stress of a fatigue cycle is reached) or where the crack faces remain in contact much longer than expected during loading. Without crack closure, one would expect the crack faces either to come into contact just when the cycles' minimum stress σ_{min} is reached or not to touch at all; without this effect, contact should occur over the entire crack face simultaneously. A variety of mechanisms of crack closure have been proposed, including: oxide or [other] particle induced closure,[158] plasticity induced closure,[159] and roughness induced closure.[160] When portions of the crack faces touch at stress $\sigma > \sigma_{min}$, the minimum stress in each fatigue cycle, further displacements of the crack faces in the vicinity of the crack tip are resisted by this local contact, so that the driving 'force' for crack extension decreases from the nominal value

of the stress intensity range $\Delta K = K_{max} - K_{min}$ to $\Delta K_{eff} < \Delta K$. The use of ΔK_{eff} or other similar functions reconciles (more or less) long and short crack rate data and explains closure's effect on crack propagation rates.[161] The fact that crack closure occurs and is important is widely accepted, even though how to measure the closure load P_{Cl} used to calculate K_{eff} is subject to considerable debate.[162–164] Normally load deflection curves of samples exhibiting crack closure show two stages, a lower slope at higher stresses and a higher slope at lower stresses; P_{Cl} is taken to be the point where the tangents to the upper and lower portions of the curves intersect.

Most studies of crack closure mechanisms have relied on observations made on the intact sample surface or on the fracture surface after testing was complete, but recently X-ray microtomography has been used to study crack closure at Al–Li 2090 T8E41, in particular with *in situ* loading so the changing pattern of openings could be followed as a function of applied load.[49,165–170] This alloy (Al–Li 2090) is particularly interesting to study because fatigue crack growth rates are much lower in the L–T orientation than in other Al alloys used in aerospace applications, and roughness induced crack closure is very pronounced in this alloy and persists to much higher stress intensity ranges than in other alloys.[171,172]

Notched tensile samples with 2·0 mm and $\sim$2·0 mm gauge and notch tip dia. respectively, were examined at four or five loads spanning the unloading portion of the fatigue cycle.[49,166–169] One set of observations was done with 22 keV synchrotron X-radiation and the second with X-rays from an Ag sealed source tube operated at 40 kV; both were reconstructed with $\sim$6 µm isotropic voxels. The fatigue cracks were rough in some places and quite planar in other parts, in agreement with crack surfaces of compact tension samples characterised with spatial and scanning electron microscopy.[163,169–178] Crack openings were quantified as a function of position for each load (Fig. 11 shows the openings measured for one sample projected on to a plane perpendicular to the load axis), and crack contact, even at the maximum stress, was observed behind the crack tip, particularly at some, but not all, positions where the crack was at its most non-planar (compare the left and right sides of the valley labelled 's' in Fig. 12). The more planar sections of the cracks zipped shut well before the microscopic closure load was reached (e.g. at 'c' in Fig. 11) while portions of the cracks remained open in the non-planar sections at stresses below the microscopic closure load. In other words mixed mode contact was important, and this is best seen in three-dimensional meshes showing crack position on which the openings (indicated by different colours) are superimposed (Fig. 12). Further, the fraction of voxels (of the original crack) open was observed to remain nearly constant on reducing the load from just above to just below the closure load; this was direct evidence that the mixed mode surface began to carry significant load at the point where the load displacement curve starts to deflect,[168] i.e. where the samples started to stiffen during unloading. These observations could not have been made without microtomography.
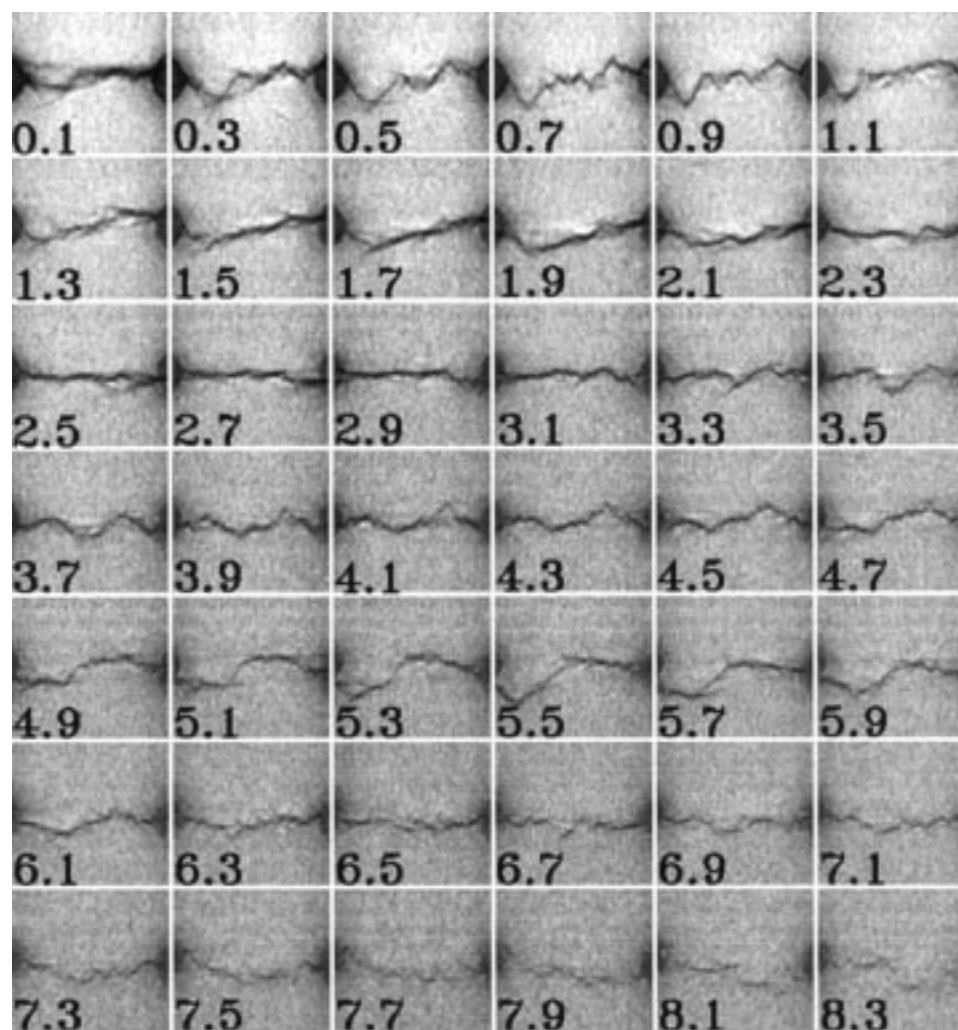
13 Sequence of cuts through Al–Li 2090 T8E41 compact tension sample containing fatigue crack. Number in lower part of each image gives distance of that cut (in mm) from tip of notch. Tips of small side grooves, separated by 1·75 mm, appear at left and right of each image, and the darker the pixel, the lower the absorption. © ICAA4, Ref. 165

Microtomographic quantification of fatigue crack opening as a function of position has also been performed in more conventional compact tension sample geometry.[165,167,170] While these samples were much smaller than normal (2–2·5 mm thick and 25·4 mm from notch tip to back face), they were scaled according to ASTM specifications and, because the entire width must be kept within the beam, this limited the voxel size to 20 μm in one case[165,167] and to 59 μm in the second.[170] An effective way of presenting the crack geometry is to show a series of equally spaced cuts spanning the length of the crack; Fig. 13 shows data from a series of 20 μm thick cuts perpendicular to the nominal crack plane and to the large faces of the compact tension sample. The multiple small asperities seen between 0·3 and 0·9 mm from the notch tip give way to a relatively planar section of the crack which extends to about 3·1 mm from the notch. Similar variation appears over the remainder of the 8·3 mm of crack which is visible.

A necessary component of the *in situ* microtomography of crack closure is use of loading apparatus. The simplest approach is to use an X-ray transparent standoff to hold the two grips apart; thin walled polycarbonate[179] or aluminium[170] tubes can provide enough rigidity and allow the sample to be viewed around 360°. The force on the sample was, in the data presented above, applied pneumatically and can also be applied by a screw mechanism much in the fashion of commercial mechanical testing apparatus. Note that simple, small and portable loading apparatus are not really suitable for growing fatigue cracks and require that a cracked specimen be dismounted from a conventional servohydraulic apparatus and remounted in the loading apparatus. Another approach employs support posts and a pair of synchronised rotators on either side of the sample; the rotators allow sample views over 360°C to be obtained without moving the posts into the beam.[105,180] The latter apparatus has the capability of testing samples to 15·6 kN.

Future directions

There is no lack of interesting materials applications for microtomography. The availability of intense, hard X-rays ($E > 50$ keV) at the newest generation synchrotron radiation sources means that more

absorbing samples such as nickel and copper can be studied. The decrease in cost of CCD camera systems as well as approaches such as time delay integration[82] increased accessibility of microtomography technology, and more research groups are finding it practical to apply it to problems that interest them.

The results reviewed above were based on measuring changes in X-ray absorptivity, but other modes of microtomography are possible. These include X-ray fluorescence, X-ray phase contrast, and X-ray diffraction microtomography. Relatively little has appeared on these topics.

X-ray fluorescence microtomography[125,181–183] requires use of a pencil beam geometry and is probably impractical unless synchrotron X-radiation is used. If one were interested in mapping the concentration of atoms of Y, an X-ray beam with photon energy $E > E(K_\alpha(Y))$ would be used. The atoms of Y within the volume traversed by the beam would fluoresce, and the signal would be collected by an energy sensitive detector placed well outside the direct beam. Correction must be made for the varying paths of the fluorescent X-rays out of the sample, and once this is done one has a quantity analogous to the line integral in equations (5) and (6). Iron in a bee's head[181] and dilute iodine based contrast media in several channels within a 12 mm acrylic cylinder[182] have been mapped with $250 \, \mu m \times 250 \, \mu m$ $1000 \, \mu m$ voxels and $\sim 10^3$ ppm sensitivity and with $1 \, mm \times 1 \, mm \times 2 \, mm$ voxels and 10^3 ng/voxel sensitivity respectively. In the latter report reconstruction was also performed with Compton scattered radiation. Thus, one of the advantages of fluorescence tomography is that much smaller concentration differences can be observed than with conventional absorption tomography. Pencil beam data collection is quite slow, fluorescence counting rates at any one position are also very low and it is difficult, in general, to compensate for the different path lengths and the potentially inhomogeneous pattern of absorption that the fluorescent X-rays must traverse on their way to the detector.

Recently there has been a strong interest in X-ray phase contrast microscopy and computed tomography because this modality (phase contrast) can be two or more orders of magnitude more sensitive than conventional attenuation constants for samples consisting of light elements.[184–187] Synchrotron radiation is required, as is an X-ray interferometer made from a monolithic block of perfect Si; Fig. 14 is a schematic showing how much an interferometer could be used for phase contrast computed tomography. One type of interferometer consists of three parallel X-ray 'half mirrors' spaced equally apart. The first crystals, diffracting in transmission, split the beam, and the resulting two beams are diffracted by the second crystal or mirror M. The beams diffracted from M are superimposed in the third crystal or analyser A and diffract once again. The result is that a pair of beams are superimposed in the direction of the beam incident on S and a second pair are superimposed along the direction of the beam diffracted from S; when no object is in one of the wave paths, the waves are in phase and there is no contrast. When an object is placed in one of the beam paths, the wavefronts
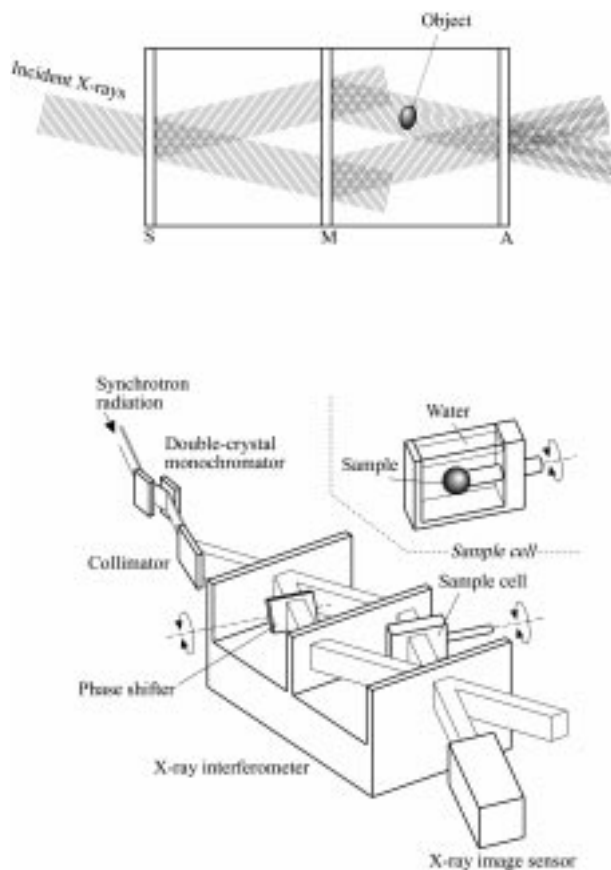
14 Illustration of interferometer (top) and apparatus (bottom) for phase contrast X-ray computed tomography. Monolithic Si crystal interferometer splits incident beam at S, split beams are diffracted again at mirror M so that they recombine at analyser A. When sample ('object' in top diagram and 'sample cell' in bottom schematic) is placed in one of beams propagating from M, phase shifts result. Insertion of phase shifter in other beam path allows one to collect enough information for each view. Reproduced with permission of SPIE from Ref. 184

are locally distorted, in a way that varies depending on what substance(s) and what path length(s) are present, i.e. on the variation of the refractive index. A number of interference images are required to obtain a single phase–contrast radiograph which can be used as one of the views required for tomographic reconstruction, but discussion of these details is beyond the scope of this brief description.[184–187] A 4 mm dia. rod-like section of the cancerous rabbit liver was imaged with 12 μm isotropic voxels, and normal tissue, fibrous tissue, cancer tissue, and degenerated cancerous lesions were clearly visible.[184] A rat cerebrum and an *intracranial* segment of rat trigeminal nerve have also been studied (2–5 mm dia. samples with 8–15 μm spatial resolutions).[185]

Light scattering in optically transparent samples is yet another way of performing microtomography,[188] but this is of only limited applicability since most engineering materials are optically opaque. X-ray diffraction can be used in a type of tomography for polycrystalline samples: the three-dimensional

variation of grain orientation, i.e. microtexture can be accurately determined[174–178,189] using polychromatic or monochromatic synchrotron X-radiation. One method of extracting the depth within a sample from which a diffracted beam originated is to record the diffracted beams on a two-dimensional detector set at a series of separations from the sample and to trace the rays back to their intersection with the incident beam (within the sample).[190–192] Domain formation *within* grains can also be mapped with X-ray microbeams; surprisingly large angle boundaries are found in the interior of grains after large strains.[193] X-ray scatter has also been used as the imaging modality.[126,194]

More and more about less and less draws finally to an end. Systematic use of X-ray microtomography in materials problems is only just beginning, and the next decade should prove very interesting indeed.

Acknowledgements

References

1. H. K. BIRNBAUM: Department of Materials Science and Engineering, University of Illinois at Urbana-Champaign, on announcing a group seminar given by S. R. Stock, 1980.
2. W. C. RÖNTGEN: *Ann. Phys. Chem.*, 1898, **64**, (1), 1–37.
3. G. HILDEBRANDT: *Int. Union Cryst.*, 1992, 27–34.
4. S. WEBB: 'From the watching of shadows: the origins of radiological tomography'; 1990, Bristol, Adam Hilger.
5. 'Compact edition of the Oxford English dictionary', Vol. III; 1987, Oxford, Clarendon Press.
6. G. GROSSMAN: *Br. J. Radiol.*, 1935, **8**, 733–751 and *Fortschr. Geb. Röntgenstr.*, 1935, **51**, 61–80.
7. J. RADON: *Ber. Sächsischen Akad. Wiss.*, 1917, **69**, 262–277. Also *IEEE Trans. Med. Imaging*, 1986, **MI-5**, (4), 170–176.
8. A. M. CORMACK: *J. Appl. Phys.*, 1963, **34**, 2722–2727.
9. G. N. HOUNSFIELD: *Br. J. Radiol.*, 1973, **46**, 1016–1022. Also UK patent 1,283,915 (1968–1972) and US patent 3,778,614 (1971–1973).
10. D. C. COPELY, J. W. EBERHARD, and G. A. MOHR: *J. Met.*, Jan. 1994, 14–26.
11. R. H. BOSSI and B. W. KNUTSON: 'The advanced development of X-ray computed tomography applications', US Air Force Wright Laboratory publication WL-TR-93-4016, February 1994.
12. U. BONSE and F. BUSCH: *Prog. Biophys. Mol. Biol.*, 1996, **65**, 133–169.
13. C. BATHIAS and A. CAGNASSO: in 'Damage detection in composite materials', ASTM STP 1128, (ed. J. E. Master), 35–54; 1992, West Conshohocken, PA, American Society for Testing and Materials.
14. M. ONOE, J. W. TSAO, H. YAMADA, H. NAKAMURA, J. KOGURE, H. KAWAMURA, and M. YOSHIMATSU: *Nucl. Instrum. Methods*, 1984, **221**, 213–230.
15. A. HABERMEHL and H.-W. RIDDER: *SPIE*, 1997, **3149**, 234–244.
16. D. H. PHILLIPS and J. J. LANNUTI: *Am. Ceram. Soc. Bull.*, 1993, **72**, 69–75.
17. W. A. ELLINGSON, P. E. ENGEL, T. I. HERTEA, K. GOPLAN, P. S. WANG, S. L. DIECKMAN, and N. GOPALSANI: in 'Industrial computed tomography', Topical Proc., 10–14, 1989, Columbus, OH, ASNT.
18. J. C. ELLIOTT and S. D. DOVER: *J. Microsc.*, 1982, **126**, 211–213.
19. T. SATO, O. IKEDA, Y. YAMAKOSHI, and M. TSUBOUCHI: *Appl. Opt.*, 1981, **20**, 3880–3883.
20. L. GRODZINS: *Nucl. Instrum. Methods*, 1983, **206**, 541–545.
21. L. GRODZINS: *Nucl. Instrum. Methods*, 1983, **206**, 547–552.
22. A. C. THOMPSON, J. LLACER, L. C. FINMAN, E. B. HUGHES, J. N. OTIS, S. WILSON, and H. D. ZEMAN: *Nucl. Instrum. Methods*, 1984, **222**, 319–323.
23. U. BONSE, Q. JOHNSON, M. NICHOLS, R. NUSSHARDT, S. KRASNICKI, and J. KINNEY: *Nucl. Instrum. Methods*, 1986, **A246**, 644–648.
24. J. H. KINNEY, Q. C. JOHNSON, U. BONSE, M. C. NICHOLS, R. A. SAROYAN, R. NUSSHARDT, R. PAHL, and J. M. BRASE: *MRS Bull.*, Jan. 1988, 13–17.
25. B. P. FLANNERY and W. G. ROBERGE: *J. Appl. Phys.*, 1987, **62**, 4668–4674.
26. B. P. FLANNERY, H. W. DECKMAN, W. G. ROBERGE, and K. L. D'AMICO: *Science*, 1987, **237**, 1439–1444.
27. P. SPANNE and M. L. RIVERS: *Nucl. Instrum. Methods*, 1987, **B24/25**, 1063–1067.
28. K. ENGELKE, M. LOHMANN, W. R. DIX, and W. GRAEFF: *Nucl. Instrum. Methods*, 1989, **A274**, 380–389.
29. K. ENGELKE, M. LOHMANN, W. R. DIX, and W. GRAEFF: *Rev. Sci. Instrum.*, 1989, **60**, 2486–2489.
30. K. UEDA, K. UMETANI, R. SUZUKI, and H. YOKOUCHI: 'A high-speed subtraction angiography system for phantom and small animal studies', Photon Factory Report, Japanese National Laboratory for High Energy Physics, KEK, 1987, 186.
31. T. HIRANO, K. USAMI, K. SAKAMOTO, and Y. SUZIKI: 'High resolution tomography employing an X-ray sensing pickup tube', Photon factory Report, Japanese National Laboratory for High Energy Physics, KEK, 1987, 187.
32. Y. SUZUKI, K. USAMI, K. SAKAMOTO, H. KOZAKA, T. HIRANO, H. SHIONO, and H. KOHNO: *Jpn J. Appl. Phys.*, 1988, **27**, L461–L464.
33. K. SAKAMOTO, Y. SUZUKI, T. HIRANO, and K. USAMI: *J. Appl. Phys.*, 1988, **27**, 127–132.
34. P. BURSTEIN, P. J. BJORKHOLM, R. C. CHASE, and F. H. SEGUIN: *Nucl. Instrum. Methods*, 1984, **221**, 207–212.
35. F. H. SEGUIN, P. BURSTEIN, P. J. BJORKHOLM, F. HOMBURGER, and R. A. ADAMS: *Appl. Opt.*, 1985, **24**, 4117–4123.
36. L. A. FELDKAMP, L. C. DAVIS, and J. W. KRESS: *J. Opt. Soc. Am.*, 1984, **A1**, 612–619.
37. L. A. FELDKAMP and G. JESION: *Rev. Prog. Quant. NDE*, 1986, **5A**, 555–566.
38. L. A. FELDKAMP, D. J. KUBINSKI, and G. JESION: *Rev. Prog. Quant. NDE*, 1988, **7A**, 381–388.
39. A. C. KAK and M. SLANEY: 'Principles of computerized tomographic imaging'; 1987, London, IEEE Press.
40. 'Annual book of ASTM standards', Vol. 03.03, 704–733; 1996, West Conshohocken, PA, ASTM.
41. 'Annual book of ASTM standards', Vol. 03.03, 784–795; 1996, West Conshohocken, PA, ASTM.
42. 'Annual book of ASTM standards', Vol. 03-03, 821–831; 1996, West Conshohocken, PA, ASTM.
43. S. R. STOCK: in 'Micromechanics: experimental techniques', AMD 102 ASME, (ed. W. N. Sharpe), 147–162; 1990, New York, ASME.
44. W. GRAEFF and K. ENGELKE: 'Handbook of synchrotron radiation', (ed. S. Ebashi *et al.*), Vol. 4, Ch. 11, 361–405; 1991, Barking, Elsevier.

45. J. H. KINNEY and M. C. NICHOLS: *Annu. Rev. Mater. Sci.*, 1992, **22**, 121–152.
46. 'Computed tomography: state of the art and future applications', (ed. T. J. Vogl *et al.*); 1996, New York, Springer-Verlag.
47. U. BONSE: *SPIE*, 1997, **3149**, 25–32.
48. B. D. CULLITY: 'Elements of X-ray diffraction'; 1978, Reading, MA, Addison-Wesley.
49. T. M. BREUNIG, S. R. STOCK, S. D. ANTOLOVICH, J. H. KINNEY, W. N. MASSEY, and M. C. NICHOLS: 'Fracture mechanics: twenty-second symposium', Vol. 1, ASTM STP 1131, (ed. H. A. Ernst *et al.*), 749–761; 1992, West Conshohocken, PA, ASTM.
50. P. M. JOSEPH: *Radiol. Skull Brain*, 1981, **5**, 3956–3997.
51. 'Donner algorithms for reconstruction tomography', described in Lawrence Berkeley Laboratory Publ. 214, 1977.
52. W. S. HADDAD and J. E. TREBES: *SPIE*, 1997, **3149**, 222–231.
53. P. D. TONNER, B. D. SWICKA, G. TOSELLO and T. ROMANINSZYN: in 'Industrial computerised tomography', 160–165; 1989, Columbus, OH, ASNT.
54. W. A. KALENDER, K. ENGELKE, and S. SCHALLER: *SPIE*, 1997, **3149**, 188–202.
55. G. WANG, P.-C. CHENG, and W. M. VANNIER: *SPIE*, 1997, **3149**, 203–212.
56. J. C. ELLIOTT and S. D. DOVER: *Metab. Bone Dis. Relat. Res.*, 1984, **5**, 219–221.
57. J. C. ELLIOTT and S. D. DOVER: *J. Microsc.*, 1985 **138**, (3), 329–331.
58. D. K. BOWEN, J. C. ELLIOTT, S. R. STOCK, and S. D. DOVER: *SPIE*, 1986, **691**, 94–98.
59. S. R. STOCK, A. GUVENILIR, T. L. STARR, J. C. ELLIOTT, P. ANDERSON, S. D. DOVER, and D. K. BOWEN: *Ceram. Trans.*, 1989, **5**, 161–170.
60. T. M. BREUNIG, J. C. ELLIOTT, P. ANDERSON, G. DAVIS, A. GUVENILIR, and S. D. DOVER: in 'New materials and their applications', Institute of Physics Conf. Series, Vol. 111, 53–60; 1990, London, Institute of Physics.
61. T. M. BREUNIG, J. C. ELLIOTT, S. R. STOCK P. ANDERSON, G. R. DAVIS, and A. GUVENILIR: in 'X-ray microscopy III', 465–468; 1992, New York, Springer-Verlag.
62. T. M. BREUNIG, S. R. STOCK, A. GUVENILIR, J. C. ELLIOTT, P. ANDERSON, and G. R. DAVIS: *Composites*, 1993, **24**, 209–213.
63. S. R. STOCK. L. L. DOLLAR, G. B. FREEMAN, W. J. READY, L. J. TURBINI, J. C. ELLIOTT, P. ANDERSON, and G. R. DAVIS: *Mater. Res. Symp. Proc.*, 1994, **323**, 65–69.
64. J. C. ELLIOTT, P. ANDERSON, G. R. DAVIS, F. S. L. WONG, and S. D. DOVER: *J. Met.*, Mar. 1994, 11–19.
65. J. C. ELLIOTT, P. ANDERSON, X. J. GAO, F. S. L. WONG, G. R. DAVIS, and S. E. P. DOWKER: *J. X-ray Sci. Technol.*, 1994, **4**, 102–117.
66. P. M. MUMMERY, B. DERBY, P. ANDERSON, G. R. DAVIS, and J. C. ELLIOTT: *J. Microsc.*, 1995, **177**, 399–406.
67. G. R. DAVIS and F. S. L. WONG: *Physiol. Meas.*, 1996, **17**, 121–146.
68. Y. I. BORODIN, E. N. DEMENTYEV, G. N. DRAGUN, G. N. KULIPANOV, N. A. MEZENTSEV, V. F. PINDYURIN, M. A. SHERMOV, A. N. SKRINSKY, A. S. SOKOLOV, and V. A. USHAKOV: *Nucl. Instrum. Methods*, 1986, **A246**, 649–654.
69. B. J. KIRBY, J. R. DAVIS, J. A. GRANT, and M. J. MORGAN: *Phys. Med. Biol.*, 1997, **42**, 1375–1385.
70. W. C. CONNER, S. W. WEBB, P. SPANNE, and K. W. JONES: *Macromol.*, 1990, **23**, 4742–4747.
71. M. A. FERRERO, R. SOMMER, P. SPANNE, K. W. JONES, and C. CONNER: *J. Polym. Sci. A*, 1993, **31**, 2507–2512.
72. B. LONDON, R. N. YANCEY, and J. A. SMITH: *Mater. Eval.*, 1990, **48**, 604–608.
73. F. A. DILMANIAN, X. Y. WU, B. REN, T. M. BUTTON, L. D. CHAPMAN, J. M. DOBBS, X. HUANG, E. L. NICKOLOFF, E. C. PARSONS, M. J. PETERSEN, W. C. TOMLINSON, and Z. ZHONG: *SPIE*, 1997, **3149**, 25–32.
74. R. NUßHARDT, U. BONSE, F. BUSCH, J. H. KINNEY, R. A. SAROYAN, and M. C. NICHOLS: *Synchrotron Radiat. News*, 1991, **4**, (3) 21–23.
75. P. ENGLER and W. D. FRIEDMAN: *Mater. Eval.*, 1990, **48**, 623–629.
76. R. A. ARMISTEAD: *Adv. Mater. Process. inc. Met. Prog.*, Mar. 1988, 41–49.
77. A. Y. SASOV: *J. Microsc.*, 1987, **147**, 169–178 and 179–192.
78. A. Y. SASOV: 'Radiation methods', 315–321; 1989, New York, Plenum Publ. Corp., translated from *Defectoskopiya*, 1988, (5), 23–30.
79. R. W. GOULET, S. A. GOLDSTEIN, M. J. CIARELLI, J. L. KUHN, M. B. BROWN, and L. A. FELDKAMP: *J. Biomech.*, 1994, **27**, 375–389.
80. U. BONSE, R. NUSSHARDT, F. BUSCH, R. PAHL, J. H. KINNEY, Q. C. JOHNSON, R. A. SAROYAN, and M. C. NICHOLS: *J. Mater. Sci.*, 1991, **26**, 4076–4085.
81. C. BUENO, M. D. BARKER, R. C. BARRY, R. A. BETZ, and S. M. JAFFEY: in Proc. 39th Int. Symp. and Exhib. of Society for the Advancement of Material and Process Engineering, April 1994, SAMPE.
82. G. R. DAVIS and J. C. ELLIOTT: *Nucl. Instrum. Methods*, 1997, **A394**, 157–162.
83. C. M. CASTELLI, J. E. ASHTON, and P. J. POOL: *SPIE*, 1997, **3149**, 92–100.
84. J. H. KINNEY, Q. C. JOHNSON, U. BONSE, R. NUSSHARDT, and M. C. NICHOLS: *SPIE*, 1986, **691**, 43–50.
85. U. BONSE, R. NUSSHARDT, F. BUSCH, R. PAHL, Q. C. JOHNSON, J. H. KINNEY, R. A. SAROYAN, and M. C. NICHOLS: *Rev. Sci. Instrum.*, 1989, **60**, 2478–2481.
86. B. ILLERHAUS, J. GOEBBELS, H. RIESEMEIER, and H. STAIGER: *SPIE*, 1997, **3149**, 101–106.
87. J. E. TREBES, K. W. DOLAN, W. S. HADDAD, J. J. HASKINS, R. A. LERCHE, C. M. LOGAN, D. E. PERKINS, D. J. SCHNEBERK, and R. D. RIKARD: *SPIE*, 1997, **3149**, 173–176.
88. G. R. DAVIS: *SPIE*, 1997, **3149**, 213–221.
89. J. O. MILEWSKI, A. B. HMELO, K. L. D'AMICO, J. H. DUNSMUIR, and S. R. FERGUSON: *Weld. J.*, Feb. 1994, 45–49.
90. W. E. KING, G. H. CAMPBELL, D. L. HAUPT, J. H. KINNEY, R. A. RIDDLE, and W. L. WIEN: *Scr. Metall. Mater.*, 1995, **33**, 1941–1946.
91. L. L. DOLLAR: 'Evaluation of nondestructive X-ray techniques for electronic packaging materials', MS thesis, Georgia Institute of Technology, Atlanta, GA, 1992.
92. C. RAVEN, A. SNIGIREV, A. KOCH, I. SNIGIREVA, and V. KOHN: *SPIE*, 1997, **3149**, 140–148.
93. J. C. ELLIOTT, P. ANDERSON, G. R. DAVIS, F. S. L. WONG, S. E. P. DOWKER, N. KOZUL, and A. BOYDE: *SPIE*, 1997, **3149**, 2–12.
94. J. H. KINNEY, T. M. BREUNIG, T. L. STARR, D. HAUPT, M. C. NICHOLS, S. R. STOCK, M. D. BUTTS, and R. A. SAROYAN: *Science*, 1993, **260**, 789–792.
95. S. B. LEE: 'Nondestructive examination of chemical vapor infiltration of 0°/90° SiC/nicalon composites', PhD thesis, Georgia Institute of Technology, Atlanta, GA, 1993.
96. S. B. LEE, S. R. STOCK, M. D. BUTTS, T. L. STARR, T. M. BREUNIG, and J. H. KINNEY: *J. Mater. Res.*, 1998, **13**, 1209–1217.
97. M. D. BUTTS: 'Nondestructive examination of nicalon fiber composite preforms using X-ray tomographic microscopy', MS thesis, Georgia Institute of Technology, Atlanta, GA, 1993.
98. T. HIRANO, K. USAMI, and K. SAKAMOTO: *Rev. Sci. Instrum.*, 1989, **60**, 2482–2485.
99. J. H. KINNEY, S. R. STOCK, U. BONSE, T. M. BREUNIG, R. A. SAROYAN, R. NUSSHARDT, Q. C. JOHNSON, F. BUSCH, and S. D. ANTOLOVICH: *J. Mater. Res.*, 1990, **5**, 1123–1129.
100. G. Y. BAAKLINI, R. T. BHATT, A. J. ECKEL, P. ENGLER, M. G. CASTELLI, and R. W. RAUSER: *Mater. Eval.*, Sep. 1995, 1040–1044.
101. T. M. BREUNIG, S. R. STOCK. J. H. KINNEY, A. GUVINILIR, and M. C. NICHOLS: *Mater. Res. Soc. Symp. Proc.*, 1991, **207**, 135–141.
102. S. R. STOCK. T. M. BREUNIG, A. GUVENILIR, J. H. KINNEY, and M. C. NICHOLS: in 'Damage detection in composite materials', ASTM STP 1128, (ed. J. E. Masters), 25–34; 1992, West Conshohocken, PA, American Society for Testing and Materials.
103. J. H. KINNEY, R. A. SAROYAN, W. N. MASSEY, M. C. NICHOLS, U. BONSE, and R. NUSSHARDT: *Rev. Prog. Quant. NDE*, 1991, **10A**, 427–433.
104. T. M. BREUNIG: 'Nondestructive evaluation of damage in SiC/Al metal matrix composite using X-ray tomographic microscopy', PhD thesis, Georgia Institute of Technology, Atlanta, GA, 1992.
105. T. HIRANO, K. USAMI, Y. TANAKA, and C. MASUDA: *J. Mater. Res.*, 1995, **10**, 381–386.
106. G. PEIX, P. CLOETENS, M. SALOMÉ, J.-Y. BUFFIÈRE, J. BARUCHEL, F. PEYRIN, and M. SCHLENKER: *SPIE*, 1997, **3149**, 149–159.
107. W. S. JOHNSON and R. R. WALLS: in 'Composite materials: fatigue and fracture', ASTM STP 907, (ed. H. Hahn), 161–175; 1986, West Conshohocken, PA, ASTM.
108. S. R. NUTT and F. E. WAWNER: *J. Mater. Sci.*, 1985, **20**, 1953.
109. B. A. LERCH, D. R. HULL, and T. A. LEONHARDT: 'As-received microstructures of a SiC/Ti-15-3 composite', NASA TM-100938, NASA, Lewis, OH, 1988.

110. J. H. KINNEY, C. HENRY, D. L. HAUPT, and T. L. STARR: *Appl. Compos. Mater.*, 1994, **1**, 325–331.
111. J. H. KINNEY and D. L. HAUPT: *J. Mater. Res.*, 1997, **12**, 610–612.
112. P. ENGLER, M. W. SANTANA, D. J. EICHENMILLER, and A. Y. SANE: in 'Industrial computed tomography II', 56–60; 1991, Columbus, OH, ASNT.
113. J. K. JASTI, G. J. JESION, and L. FELDKAMP: *SPE Formation Eval.*, Sep. 1993, 189–193.
114. F. M. AUZERAIS, J. DUNSMUIR, B. B. FERREOL, N. MARTYS, J. OLSON, T. S. RAMAKRISHAN, D. H. ROTHMAN, and L. M. SCHWARTZ: *Geophys. Res. Lett.*, 1996, **23**, 705–708.
115. L. M. SCHWARTZ, F. AUZERAIS, J. DUNSMUIR, N. MARTYS, D. P. BENTZ and S. TORQUATO: *Physica A*, 1994, **207**, 28–36.
116. P. SPANNE, J. F. THORVERT, C. J. JACQUIN, W. B. LINDQUIST, K. W. JONES, and P. M. ADLER: *Phys. Rev. Lett.*, 1994, **73**, 2001–2004.
117. J. H. DUNSMUIR, M. ZHOU, B. P. FLANNERY, M. AMABILE, A.-M. LANZILLOTTO, T. S. LEU, R. SAMTANEY, and R. WILDES: *SPIE*, 1997, **3149**, 82–89.
118. T. L. STARR: *Mater. Res. Soc. Symp. Proc.*, 1992, **250**, 207.
119. W. J. READY, L. J. TURBINI, S. R. STOCK, and B. A. SMITH: in Proc. 34th IEEE Reliability Physics Symp., 267–273; 1996, London, IEEE.
120. J. H. KINNEY, N. E. LANE, and D. L. HAUPT: *J. Bone Miner. Res.*, 1995, **10**, 264–270.
121. A. ODGAARD and H. J. G. GUNDERSON: *Bone*, 1993, **14**, 173–182.
122. K. ENGELKE, W. GRAEFF, L. MEISS, M. HAHN, and G. DELLING: *Invest. Radiol.* 1993, **28**, 341–349.
123. E. L. RITMAN, S. M. JORGENSEN, P. E. LUND, P. J. THOMAS, J. H. DUNSMUIR, J. C. ROMERO, R. T. TURNER, and M. E. BOLANDER: *SPIE*, 1997, **3149**, 13–24.
124. J.-L. KUHN, S. A. GOLDSTEIN, L. A. FELDKAMP, R. W. GOULET, and G. JESION: *J. Orthop. Res.*, 1990, **8**, 833–842.
125. H. YASUMUIRA, K. JONES, P. SPANNE, G. SCHIDLOVSKY, L. WIELOPOLSKI, X. REN, D. GLAROS, and Y. XATZIKONSTANINOU: *J. Nutr.*, 1993, **123**, 459–464.
126. U. KLEUKER and C. SCHULZE: *SPIE*, 1997, **3149**, 177–185.
127. J. M. FEARNE, J. C. ELLIOTT, F. S. L. WONG, G. R. DAVIS, A. BOYDE, and S. J. JONES: *Anat. Embryol.*, 1994, **189**, 375–381.
128. H. D. ZEMAN, E. B. HUGHES, L. C. FINMAN, R. HOFSTADTER, A. HUDSON, J. N. OTIS, J. ROLFE, E. RUBENSTEIN, D. C. HARRISON, R. S. KERNOFF, A. C. THOMPSON, and G. S. BROWN: *Nucl. Instrum. Methods*, 1984, **222**, 308–318.
129. J. C. ELLIOTT, T. G. BROMAGE, P. ANDERSON, G. DAVIS, and S. D. DOVER: in 'Enamel V', (ed. R. W. Feanhead), 429–433; 1989.
130. F. S. L. WONG, J. C. ELLIOTT, P. ANDERSON, and G. R. DAVIS: *J. Dent. Res.*, 1991, **70**, 691.
131. F. S. L. WONG, J. C. ELLIOTT, P. ANDERSON, and G. R. DAVIS: *Bone*, 1995, **16**, 690.
132. F. S. L. WONG, J. C. ELLIOTT, P. ANDERSON, and G. R. DAVIS: *J. Dent. Res.*, 1995, **74**, 849.
133. J. C. ELLIOTT, P. ANDERSON, G. R. DAVIS, F. S. L. WONG, X. J. GAO, S. D. DOVER, and A. BOYDE: in 'X-ray microscopy III', (ed. A. Michette *et al.*), 461–464; 1992, Berlin, Springer-Verlag.
134. J. H. KINNEY, G. W. MARSHALL Jr, and S. J. MARSHALL: *Scanning Microsc.*, 1994, **8**, 197–205.
135. C. E. MERCER and P. ANDERSON: *J. Dent. Res.*, 1995, **74**, 849.
136. R. B. NEILSEN, A. M. ALLYASSIH, D. D. PETERS, D. CARNES, and J. LANCASTER: *J. Endod.*, 1995, **21**, 561–568.
137. S. E. P. DOWKER, G. R. DAVIS, and J. C. ELLIOTT: *Oral Surg. Oral Med. Oral Pathol. Oral Radiol. Endod.*, 1997, **83**, 510–516.
138. F. S. L. WONG, J. C. ELLIOTT, A. ANDERSON, and G. R. DAVIS: *Calcif. Tissue Int.*, 1995, **56**, 62–70.
139. J. C. ELLIOTT, P. ANDERSON, G. R. DAVIS, F. S. L. WONG, X. J. GAO, S. D. DOVER, and A. BOYDE: in 'X-ray microscopy III', (ed. A. Mitchette *et al.*), 461–464; 1992, Berlin, Springer-Verlag.
140. G. L. MECHANIC, S. B. ARNAUD, A. BOYDE, T. G. BROMAGE, P. BUCKENDAHL, J. C. ELLIOTT, E. P. KATZ, and G. N. DURNOVA: *FASEB J.*, 1990, **4**, 34–40.
141. F. PEYRIN, M. SALOMÉ, F. DENIS, P. BRAILLON, A.-M. LAVAL-JEANLET, and P. CLOETENS: *SPIE*, 1997, **3149**, 44–52.
142. M. W. LAYTON, S. A. GOLDSTEIN, R. W. GOULET, L. A. FELDKAMP, D. J. KUBINSKI, and G. G. BOLE: *Arthritis Rheum.*, 1988, **31**, 1400–1405.
143. D. K. DEDRICK, R. GOULET, L. HUSTON, S. A. GOLDSTEIN, and G. G. BOLE: *J. Rheumatol. Suppl.*, 1991, **27**, 44–45.
144. D. K. DEDRICK, S. A. GOLDSTEIN, K. D. BRANDT, B. L. O'CONNOR, R. W. GOULET, and M. ALBRECHT: *Arthritis Rheum.*, 1993, **36**, 1460–1467.
145. U. BONSE, F. BUSCH, O. GUNNEWIG, F. BECKMANN, R. PAHL, G. DELLING, M. HAHN, and W. GRAEFF: *Bone Miner.*, 1994, **25**, 25–38.
146. L. A. FELDKAMP, S. A. GOLDSTEN, A. M. PARFITT, G. JESION, and M. KLEEREKOPES: *Bone Miner. Res.*, 1989, **4**, 3–11.
147. A. J. C. LADD and J. H. KINNEY: *Physica A*, 1997, **240**, 349–360.
148. S. A. GOLDSTEIN, R. GOULET, and D. McCUBBREY: *Calcif. Tissue Int.*, 1993, **53**, Suppl. 1, S127–S133.
149. J. H. KINNEY, N. LANE, S. MAJUMDAR, S. J. MARSHALL, and G. W. MARSHALL: *J. Bone Miner. Res.*, 1992, **7**, Supp. 1, S136.
150. T. HILDEBRAND, A. LAIB, D. ULRICH, A. KOHLBRENNER, and P. RÜEGSEGGER: *SPIE*, 1997, **3149**, 34–43.
151. K. ENGELKE, G. UMGIEßER, S. PREVRHAL, and W. KALENDAR: *SPIE*, 1997, **3149**, 53–61.
152. J. H. KINNEY, D. L. HAUPT, and A. J. C. LADD: *SPIE*, 1997, **3149**, 64–68.
153. R. MÜLLER and W. C. HAYES: *SPIE*, 1997, **3149**, 69–81.
154. D. D. CODY, D. A. McCUBBREY, G. W. DIVINE, G. J. GROSS, and S. A. GOLDSTEIN: *J. Biomech.*, 1996, **29**, 753–761.
155. J. L. KUHN, R. W. GOULET, M. PAPPAS, and S. A. GOLDSTEIN: *J. Orthop. Res.*, 1990, **8**, 776–780.
156. U. BONSE, F. BUSCH, O. GUNNEWIG, F. BECKMANN, G. DELLING, M. HAHN, and A. KVICK: *ESRF Newsl.*, Mar. 1996, 21–23.
157. R. E. GULDBERG, N. J. CALDWELL, X. E. GUO, R. W. GOULET, S. J. HOLLISTER, and S. A. GOLDSTEIN: *J. Bone Miner. Res.*, 1997, **12**, 1295–1302.
158. R. H. CHRISTENSEN: *Appl. Mater. Res.*, Oct. 1963, 207–210.
159. W. ELBER: in 'Damage tolerance in aircraft structures', ASTM STP 486, 230–242; 1971, West Conshohocken, PA, ASTM.
160. S. SURESH and R. O. RITCHIE: *Met. Trans.*, 1982, **13A**, 1627–1631.
161. S. SURESH, G. F. ZANISKI, and R. O. RITCHIE: *Met. Trans.*, 1981, **12A**, 1435–1443.
162. D. E. MACHA, D. M. CORBLY, and J. W. JONES: *Exp. Mech.*, 1979, **19**, 207–213.
163. M. E. FINE, J. L. HORNG, and D. H. PARK: 'Fatigue 84', (ed. C. J. Beevers), Vol. II, 739–748; 1984, Warley, Engineering Materials Advisory Services.
164. K. TOKAJI, Z. ANDO, J. NAGAE, and T. IMAI: in 'Fatigue 84', (ed. C. J. Beevers), Vol. II, 739–748; 1984, Warley, Engineering Materials Advisory Services.
165. A. GUVENILIR, S. R. STOCK, M. D. BARKER, and R. A. BETZ: in Proc. 4th Int. Conf. on 'Aluminum alloys: their physical properties and mechanical properties', Vol. II, 413–419; 1994, Atlanta, GA, Georgia Institute of Technology.
166. S. R. STOCK, A. GUVENILIR, T. M. BREUNIG, J. H. KINNEY, and M. C. NICHOLS: *J. Met.*, Jan 1995, 19–24.
167. A. GUVENILIR: 'Investigation into asperity-induced closure in an Al–Li alloy using X-ray tomography', PhD thesis, Georgia Institute of Technology, Atlanta, GA, 1995.
168. A. GUVENILIR, T. M. BREUNIG, J. H. KINNEY, and S. R. STOCK: *Acta Mater.*, 1997, **45**, 1977–1987.
169. A. GUVENILIR and S. R. STOCK: *Fatigue Fract. Eng. Mater. Struct.*, 1998, **21**, 439–450.
170. R. MORANO, S. R. STOCK, G. R. DAVIS and J. C. ELLIOTT: unpublished data, 1998. Also, R. MORANO: 'Effect of *R*-ratio on crack closure in Al–Li 2090 T8E41, investigated non-destructively with X-ray micro-tomography', MS thesis, Georgia Institute of Technology, Atlanta, GA, 1998.
171. K. T. VENKATESWARA RAO, W. YU, and R. O. RITCHIE: *Met. Trans.*, 1988, **19A**, 549–561 and 563–569.
172. P. S. PAO, L. A. COOLEY, M. A. IMAM, and G. R. YODER: *Scr. Metall.*, 1989, **23**, 1455–1460.
173. H. Y. JUNG: 'Characterization of fatigue crack propagation in Al–Li 2090 alloys', PhD thesis, Georgia Institute of Technology, Atlanta, GA, 1994.
174. J. D. HAASE, D. P. PIOTROWSKI, A. GUVENILIR, J. R. WITT, and S. R. STOCK: *Adv. X-ray Anal.*, 1999, **41**, 188–194.
175. J. D. HAASE: 'Microbeam diffraction mapping of microtexture in Al–Li 2090 T8E41', MS thesis, Georgia Institute of Technology, Atlanta, GA, 1998.
176. J. D. HAASE, A. GUVENILIR, J. R. WITT, and S. R. STOCK: *Acta Mater.*, 1998, **46**, 4791–4799.
177. J. D. HAASE, A. GUVENILIR, J. R. WITT, and S. R. STOCK: *Mater. Res. Soc. Proc.*, 1998, **524**, 37–42.
178. J. D. HAASE, A. GUVENILIR, J. R. WITT, M. A. LANGØY, and S. R. STOCK: in 'Mixed-mode crack behavior', ASTM STP 1359, 160–173; 1999, West Conshohocken, PA, ASTM.
179. T. M. BREUNIG, S. R. STOCK, and R. C. BROWN: *Mater. Eval.*, May 1993, 596–600.

180. T. M. BREUNIG, M. C. NICHOLS, J. S. GRUVER, J. H. KINNEY, and D. L. HAUPT: *Ceram. Eng. Sci. Proc.*, 1994, **15**, 410–417.
181. P. BOISSEAU and L. GRODZINS: *Hyperfine Interact.*, 1987, **33**, 283–292.
182. T. TAKEDA, M. AKIBA, T. YUASA, M. KAZAMA, A. HOSHINO, Y. WATANABE, K. HYODO, F. A. DILMANIAN, T. AKATSUKA, and Y. ITAI: *SPIE*, 1996, **2708**, 685–695.
183. T. TAKEDA, T. YUASA, A. HOSHINO, M. AKIBA, A. UCHIDA, M. KAZAMA, K. HYODO, F. A. DILMANIAN, T. AKATSUKA, and Y. ITAI: *SPIE*, 1997, **3149**, 160–172.
184. A. MOMOSE, T. TAKEDA, Y. ITAI, and K. HIRANO: *SPIE*, 1996, **2708**, 674–684.
185. F. BECKMANN, U. BONSE, F. BUSCH, and O. GUNNEWIG: *J. Comput. Assist. Tomogr.*, 1997, **21**, 539–553.
186. U. BONSE, F. BECKMANN, M. BARTSCHER, T. BEIRMANN, F. BUSCH, and O. GÜNNEWIG: *SPIE*, 1997, **3149**, 108–119.

187. A. MOMOSE, T. TAKEDA, and Y. ITAI: *SPIE*, 1997, 120–129.
188. W. J. P. van ENCKEVORT and H. G. M. LOCHS: *J. Appl. Phys.*, 1988, **64**, 434–437.
189. H. F. POULSEN, S. GARBE, T. LORENTZEN, D JUUL JENSEN, F. W. POULSEN, N. H. ANDERSON, T. FRELLO, R. FEIDENHANS'L, and H. GRAAFSMA: *J. Synchrotron Radiat.*, 1997, **4**, 147–154.
190. S. R. STOCK, A. GUVENILIR, D. P. PIOTROWSKI, and Z. U. REK: *Mater. Res. Soc. Proc.*, 1995, **375**, 275–280.
191. D. P. PIOTROWSKI, S. R. STOCK, A. GUVENILIR, J. D. HAASE, and Z. U. REK: *Mater. Res. Soc. Proc.*, 1997, **427**, 125–128.
192. D. P. PIOTROWSKI: 'Synchrotron polychromatic X-ray diffraction tomography of large-grained polycrystalline materials', MS thesis, Georgia Institute of Technology, Atlanta, GA, 1996.
193. G. C. BUTLER, A. GUVENILIR, D. L. MCDOWELL, and S. R. STOCK: *Mater. Res. Soc. Proc.*, 1998, **524**, 43–48.
194. U. KLEUKER: *SPIE*, 1997, **3149**, 245–256.